Title

Algorithmic and Visual Aids for Physical Discovery Using Bispectral Mode Decomposition

Author

Gonzalez, Juan Amilcar

Publication Date

2023

Peer reviewed|Thesis/dissertation

UNIVERSITY OF CALIFORNIA SAN DIEGO

Algorithmic and Visual Aids for Physical Discovery Using Bispectral Mode Decomposition

A thesis submitted in partial satisfaction of the
requirements for the degree Master of Science

in

Engineering Science (Aerospace Engineering)

by

Juan A. Gonzalez

Committee in charge:

Professor Oliver T. Schmidt, Chair
Professor Keiko K. Nomura
Professor Sutanu Sarkar

2023

The thesis of Juan A. Gonzalez is approved, and it is acceptable in quality and form for publication on microfilm and electronically.

University of California San Diego

2023

DEDICATION

To all first generation college students.

EPIGRAPH

Once more unto the breach, dear friends, once more.

William Shakespeare, Henry V

TABLE OF CONTENTS

LIST OF FIGURES

LIST OF TABLES

ACKNOWLEDGEMENTS

First, I would like to extend my deepest gratitude to my advisor Professor Oliver T. Schmidt. I am forever in his debt and am truly thankful that he ever considered giving me the opportunity to conduct research in his group. Schmidt's guidance, support, and teachings have helped me grow immensely as both a student and researcher.

I am also grateful for all those in the lab during my time in the graduate program. Akhil, Tianyi, Edward, Brandon, Cong, and Ethan were all wonderful to work with. I thoroughly enjoyed the time I had with the lab and could never ask for a better environment.

And lastly, I am grateful for those in my personal life that have helped me in ways that I could never repay. My parents for supporting me as I furthered my education in this endeavor into graduate school, and for my partner, Sophia. Her love, support, and motivation were the only reasons I was able to continue this program when I was plagued with self-doubt. Without her, this work would never have come into fruition.

ABSTRACT OF THE THESIS

Algorithmic and Visual Aids for Physical Discovery Using Bispectral Mode Decomposition

by

Juan A. Gonzalez

Master of Science in Engineering Science (Aerospace Engineering)

University of California San Diego, 2023

Professor Oliver T. Schmidt, Chair

Triadic interactions are the fundamental mechanism of energy transfer in fluid flows and arise due to the quadratic non-linearity of the Navier-Stokes equation. The bispectral mode decomposition (BMD) is a direct means of revealing flow structures that are associated with these interactions and accomplishes this by computing modes generated by the interaction of two separate modes. The mode bispectrum, summed mode spectrum, and bispectral modes are the primary results produced through the use of the BMD, with local maxima in the mode bispectrum and summed mode spectrum representing the most prominent triadic interactions of the flow.

However, these results are often difficult to analyze due to uncertainty in determining

what constitutes a local maxima. In this work, a radial search algorithm that has been developed is applied to both the mode bispectrum and summed mode spectrum of open cavity flow data to find their respective maxima. Once found, these maxima are reconstructed into two new visual aids, the sparse mode bispectrum and an arrangement of the bispectral modes. The sparse mode bispectrum condenses the results of radially searching the mode bispectrum and summed mode spectrum, while local maxima found through the radial search of the mode bispectrum have their corresponding bispectral modes arranged in the relative shape of the mode bispectrum. These visualizations aim to present the most important information and results from the BMD according to the radial search algorithm, allowing for the identification of the most pertinent flow physics while also easing the use of the BMD.

Chapter 1

Background

The turbulent energy cascade, a concept first presented by Richardson [20] with the first statistical theory proposed by Kolmogorov [10], describes the energy transfer from larger scales of motion to smaller scales. This energy cascade is a consequence of the triadic interactions found in fluid flows which arise due to the quadratic non-linearity of the Navier-Stokes equations. Introduced by Kraichnan's cornerstone works [11] [12], these triadic interactions, in Fourier space, are wavenumber triplet vectors $\{\mathbf{k}_j, \mathbf{k}_k, \mathbf{k}_l\}$, or frequencies, $\{f_j, f_k, f_l\}$, that sum to zero:

$$\mathbf{k}_j \pm \mathbf{k}_k \pm \mathbf{k}_l = \mathbf{0}, \tag{1.1}$$

$$f_j \pm f_k \pm f_l = 0. \tag{1.2}$$

Triadic interactions in turbulent flows have since been the subject of many studies and investigations. Domaradzki et al [4] concluded that nonlocal energy transfers from large scales to small scales in incompressible turbulent flows with high Reynolds numbers and from small to large scales at low Reynolds numbers. Minnie et al [17] showed that the large scale flow plays an important role in the development and the statistical properties of the small scale turbulence. Furthermore, non-linear triadic interactions have been showcased by Farazmand and Sapsis [5] to cause extreme dissipation events due to the spontaneous transfer of energy from large scales to the mean flow via non-linear triad interactions. Indeed, it becomes clear that triadic interactions

are the fundamental mechanism of energy transfer in fluid flows.

The bispectral mode decomposition (BMD) is a modal decomposition technique that directly extracts flow structures associated with triadic interactions [25]. Other decomposition methods, such as the proper orthogonal decomposition (POD) [1] and dynamic mode decomposition (DMD) [23], have been used to decompose flow data into coherent structures [24]. Such decomposition methods, however, are not inherently designed to account for the non-linearity present from triadic interactions. Therefore, electing to utilize the BMD on flow data may provide new insight previously missed due to this crucial characteristic of the method.

In this work, the BMD will be applied to direct numerical simulation (DNS) data of an open cavity flow. Key results of the BMD, in particular the mode bispectrum and summed mode spectrum, can often be difficult to interpret due to difficulty in determining their local maxima. These maxima in the mode bispectrum are of interest as they identify quadratically interacting frequency components. A radial search algorithm has been developed and applied to both the mode bispectrum and summed mode spectrum to aid in determining their respective maxima. Once found, these maxima are reconstructed into two new visualizations that contain the most relevant results from the BMD, allowing for the identification of the most pertinent flow physics.

However, as the DNS of an open cavity flow is the numerical data analyzed by the BMD and radial search algorithm, we take the time now to discuss its formulation and expected physical phenomena. Discussion behind the mathematics and characteristics of the BMD, radial search algorithm, and visualizations are reserved for Chapter 2; they are the core methods behind the analysis presented in this work.

1.1 Direct Numerical Simulation

Direct numerical simulation (DNS) is a technique used to study flows of particular interest by directly solving the Navier-Stokes equations numerically without any turbulence model; i.e, turbulence is explicitly resolved [3]. As this simulation is computationally expensive,

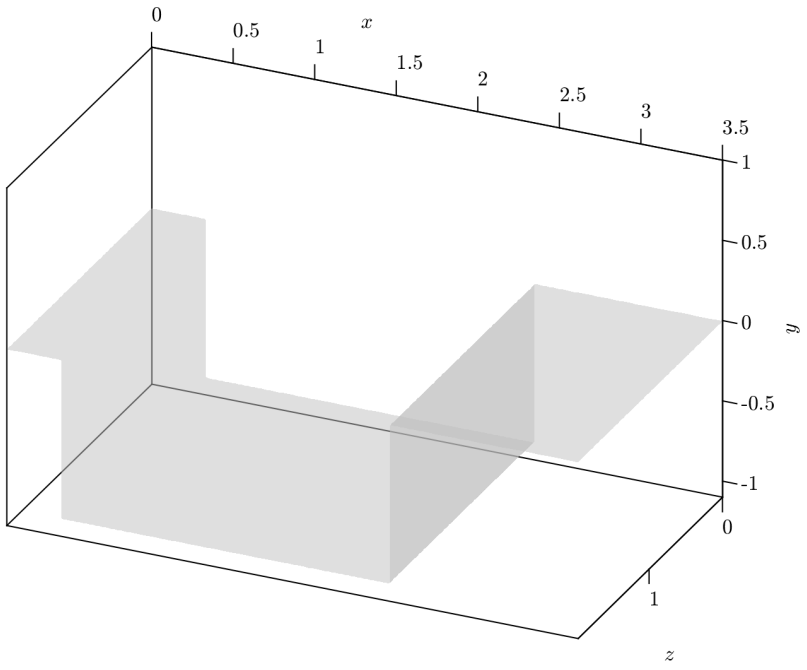

Figure 1.1. Visulization of the open cavity used in the DNS. The spanwise direction (z) is spatially homogeneous and restricted to a domain of $z \in [0, 1.9688]$ as shown.

the physical region that is simulated often tends to be quite small [19]. However, studies of DNS of open cavity flows are not new and have been analyzed with various fluid flow conditions and geometries. Studies have analyzed DNS of open cavity flow with conditions such as high speed flow [6], subsonic flow [27], and cubical open cavities [13].

The DNS data of the open cavity was provided by Professor Medeiros' lab from the University of São Paulo. The streamwise direction of the flow in the open cavity will be defined as the x-axis, the transverse direction y-axis, and the spanwise direction as the z-axis. The spanwise direction will be assumed spatially invariant with a domain of $z \in (-\infty, \infty)$, but as this is in practice periodic, the DNS considers z to be in the domain $z \in [0, 1.9688]$. Table 1.1 showcases how the open cavity is discretized for the DNS while Figure 1.1 is a visualization of the open cavity without any flow.

Besides the physical domain of the open cavity, the fluid parameters used are also relevant for the DNS. The fluid used for the simulation is air at an initial temperature $300K$. Table 1.2 lists

Table 1.1. Discretization of the open cavity for the DNS. The length-depth ratio, L/D, is 2. Dimensional units are normalized by depth.

Axis	Nodes	Domain	Nodes in Cavity	Domain of Cavity
x	$N_x = 216$	$x \in [-1.6598, 6.3402]$	$N_x = 99$	$x \in [0.304, 2.304]$
y	$N_y = 186$	$y \in [-1, 4]$	$N_y = 82$	$y \in [0, -1]$
z	$N_z = 64$	$z \in [0, 1.9688]$	$N_z = 64$	$z \in [0, 1.9688]$

Table 1.2. Flow parameters used in the DNS of the open cavity flow.

Flow Parameter	Value
Reynolds (characterized by depth, ReD)	1500
Mach (Ma)	0.5
Specific heat ratio (γ)	1.4
Prandtl (Pr)	0.71
Initial temperature (T_0)	$300K$

relevant fluid flow parameters used in the DNS. For more details on the methodology behind the DNS of the open cavity, readers are directed towards works such as [14] and [15] by Professor Medeiros and Mathias. Insight is provided into the schemes used for their numerical simulation process, along with mesh and domain convergence analysis. Several DNS open cavity flow cases similar to the one presented here are discussed at length in those works.

This is not to say that the BMD was immediately applied to the DNS data in its current state. Due to the spatial homogeneity available in the z-axis of the open cavity, the discrete Fourier transformation (DFT) in the z-direction can be utilized to transform the DNS data to wavenumber space. Using MATLAB's `fft` function, this entails implementing

$$X[k+1] = \sum_{n=0}^{N-1} x(n+1) W_N^{k_n}, \tag{1.3}$$

where $W_n = e^{-j\frac{2\pi}{N}}$ [8]. Notably, indexing starts at one instead of zero due to MATLAB's indexing convention. Using the DFT leads to a reduction from three-dimensions to two-dimensions. This is useful for increasing computational efficiency, convergence of spectral estimates, and

interpretability [25]. The wavenumbers we will be considering are wavenumbers $k_z \leq 3$, where k_z are the spanwise wavenumbers in the z-direction and are nonnegative integer values. How the use of the DFT affects the mathematics behind the BMD will be explored in Chapter 2, section 1. For now, we move on and discuss physical phenomena that is expected to arise due to the geometry of the flow.

1.2 Rossiter Modes

As the simulation described in the previous section is of an open cavity flow with a short cavity, $L/D = 2$, we expect there to be Rossiter modes in the spectrums produced by the BMD. Rossiter modes are the frequencies that correspond to large-amplitude, self-sustained oscillations of the pressure, velocity, and density fields in and around the cavity [9]. They are caused by the shear layer spanning across the cavity (which separates the cavity from external flow) rolling into discrete vortices colliding with the cavity trailing edge. This disturbance propagates upstream and interacts with the cavity leading edge producing new vortices and starting the cycle once more. Figure 1.2 is a two-dimensional schematic of the open cavity flow that showcases this phenomena occurring at an arbitrary time.

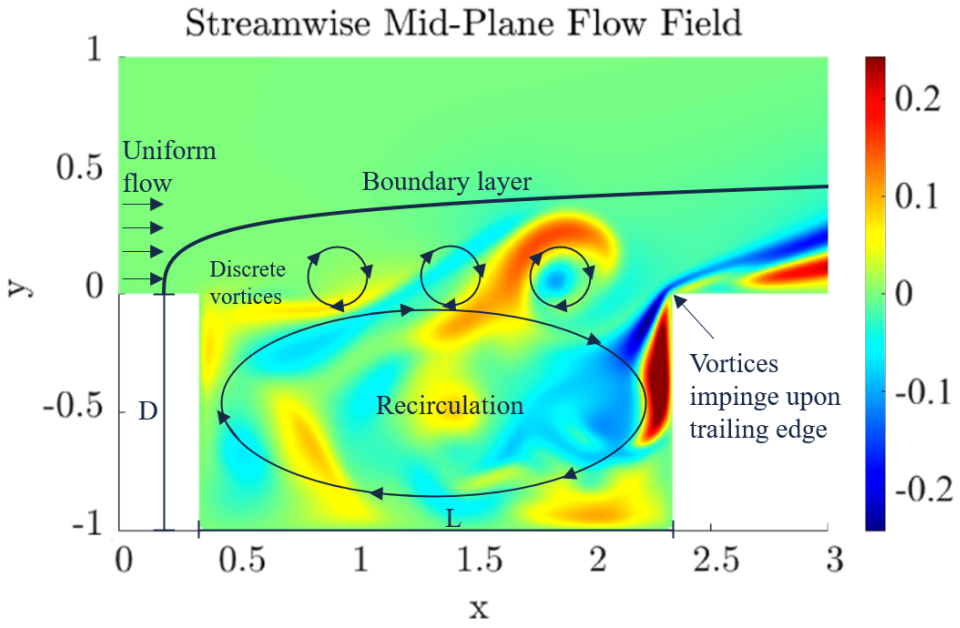

Figure 1.2. Schematic of the open cavity flow showcasing the Rossiter mode feedback loop. This snapshot is taken at the mid-plane of the open cavity geometry and shows the streamwise velocity at an arbitrary time.

Rossiter modes are named after J. E. Rossiter [22] who was the first author that studied this phenomena and proposed an empirical equation that accurately predicts the frequencies these oscillations occur. The equation is the following,

$$f = \frac{U(m-\gamma)}{L(\frac{1}{K}+Ma)}, \tag{1.4}$$

where f is the frequency, L is the length of the cavity, γ and K are empirical constants, Ma is the tunnel Mach number, U is the tunnel speed, and m is an integer 1, 2, ..., etc that corresponds to the Rossiter mode being predicted. This means that $m = 1$ corresponds to the first Rossiter mode, $m = 2$ corresponds to the second Rossiter mode, and so on. For the empirical constants, $\gamma = 0.25$ for an open cavity with $L/D = 2$ while $K = 0.57$ in general. The predicted Rossiter mode frequencies will be compared with the frequencies found using the BMD in Chapter 3. The frequency triads corresponding to Rossiter modes will be of particular interest.

Chapter 2

Methods

First, flow structures associated with triadic interactions are extracted using the BMD. Once the modal decomposition is complete, we sift through the results using a radial search algorithm to determine the location of local maxima and therefore, the frequencies that correspond to the most prominent triadic interactions. Following the steps of this process, we will first discuss the mathematics behind the BMD and then the radial search algorithm.

2.1 Bispectral Mode Decomposition

Triadic interactions are characterized by quadratic phase coupling which can be detected by the bispectrum, but unlike the classical bispectrum, the BMD establishes a casual relationship between the three frequency components of a triad. The BMD accomplishes this by computing modes associated with frequency triads as well as computing a mode bispectrum that identifies resonant three-wave interactions. This requires modes that exhibit quadratic phase coupling over extended portions of the flow field. To compute such modes, the decomposition optimally represents the data in terms of an integral measure of the bispectral density between two frequency interactions. Mathematically, the integral measure is the following,

$$b(f_k, f_l) \equiv E\left[\int_\Omega \hat{\mathbf{q}}_k^* \circ \hat{\mathbf{q}}_l^* \circ \hat{\mathbf{q}}_{k+l}\, d\mathbf{x}\right] = E\left[\hat{\mathbf{q}}_{k\circ l}^H \mathbf{W} \hat{\mathbf{q}}_{k+l}\right] = E\left[\hat{\mathbf{q}}_{k\circ l}, \hat{\mathbf{q}}_{k+l}\right], \tag{2.1}$$

where $\mathbf{W}$ is the diagonal matrix of spatial quadrature weights and Ω is the spatial domain over which the flow is defined. The operations $(.)^*$, $(.)^T$, and $(.)^H$ correspond to the scalar complex conjugate, transpose, and complex transpose, respectively.

We then take into account the casual relation between the sum-frequency component and the product of the l-th and k-th frequency components that form a resonant triad and define two linear expansions:

$$\phi_{k\circ l}^{[i]}(\mathbf{x}, f_k, f_l) = \sum_{j=1}^{N_{blk}} a_{ij}(f_{k+l})\hat{\mathbf{q}}_{k\circ l}^{[j]}, \tag{2.2}$$

$$\phi_{k+l}^{[i]}(\mathbf{x}, f_k, f_l) = \sum_{j=1}^{N_{blk}} a_{ij}(f_{k+l})\hat{\mathbf{q}}_{k+l}^{[j]}, \tag{2.3}$$

that share a common set of expansion coefficients a_{ij}. ϕ_{k+l} is of particular interest as these are the bispectral modes of the BMD and reveal the flow structures that are generated through triadic interactions. Certain bispectral modes computed from the data set will be shown and discussed in Chapter 3, section 4. $\phi_{k\circ l}$, on the other hand, are multiplicative cross-frequency fields and are maps of phase-alignment between two frequency components that many not be directly observed. While they are computed during the use of the BMD on the data set, they are not a focus in our analysis and as such will not be discussed further.

We can equations rewrite equations 2.2 and 2.3 in a more compact manner through the following,

$$\phi_{k\circ l}^{[i]} = \hat{\mathbf{Q}}_{k\circ l}\mathbf{a}_i, \tag{2.4}$$

$$\phi_{k+l}^{[i]} = \hat{\mathbf{Q}}_{k+l}\mathbf{a}_i, \tag{2.5}$$

where $\mathbf{a}_i = [a_{i1}(f_{k+l}), a_{i1}(f_{k+l}), \cdots, a_{iN_{blk}}(f_{k+l})]^T$ denotes the i-th vector of expansion coeffi-

cients for the (k,l) frequency doublet and $\hat{\mathbf{Q}}$ are data matrices of the form

$$\hat{\mathbf{Q}}_{k\circ l} = \begin{bmatrix} | & | & & | \\ \hat{\mathbf{q}}_{k\circ l}^{[1]} & \hat{\mathbf{q}}_{k\circ l}^{[2]} & \cdots & \hat{\mathbf{q}}_{k\circ l}^{[N_{blk}]} \\ | & | & & | \end{bmatrix}, \tag{2.6}$$

$$\hat{\mathbf{Q}}_{k+l} = \begin{bmatrix} | & | & & | \\ \hat{\mathbf{q}}_{k+l}^{[1]} & \hat{\mathbf{q}}_{k+l}^{[2]} & \cdots & \hat{\mathbf{q}}_{k+l}^{[N_{blk}]} \\ | & | & & | \end{bmatrix}. \tag{2.7}$$

To compute modes that optimally represent the data in terms of the bispectral density, we seek the set of expansion coefficients $\mathbf{a}_1$ that maximizes the absolute value of $b(f_k, f_l)$ in 2.1. The optimal

$$\mathbf{a}_1 = \arg\max_{\|\mathbf{a}\|=1} \left| E\left[\phi_{k\circ l}^{[1]H} \mathbf{W} \phi_{k+l}^{[1]}\right]\right|, \tag{2.8}$$

which can be simplified and thus written compactly as,

$$\mathbf{a}_1 = \arg\max \left| \frac{\mathbf{a}^H \mathbf{B} \mathbf{a}}{\mathbf{a}^H \mathbf{a}} \right|, \tag{2.9}$$

by introducing,

$$\mathbf{B} = \mathbf{B}(\mathbf{x}, \mathbf{x}', f_k, f_l) \equiv \frac{1}{N_{blk}} \hat{\mathbf{Q}}_{k\circ l}^H \mathbf{W} \hat{\mathbf{Q}}_{k+l}, \tag{2.10}$$

as the weighted bispectral density.

This problem is directly related to the numerical range of the weighted bispectral density and therefore the largest absolute value the numerical range can attain defines the numerical radius to be

$$r(\mathbf{B}) = \max |\lambda| : \lambda \in F(\mathbf{B}). \tag{2.11}$$

Finally, it has been shown before [28][21] that the numerical radius corresponds to the largest

eigenvalue, λ_{max}, that the Hermitian matrix,

$$\mathbf{H}(\theta) = \frac{1}{2}(e^{i\theta}\mathbf{B} + e^{-i\theta}\mathbf{B}^H), \tag{2.12}$$

can attain for some angle $0 \leq \theta < 2\pi$, i.e.,

$$r(\mathbf{B}) = \max_{0 \leq \theta < 2\pi} \lambda_{max}(\mathbf{H}(\theta)), \tag{2.13}$$

which is chosen to be solved with an efficient algorithm such as He and Waston's [7] rather than through a brute-force method that discretizes the interval $\theta \in (0, 2\pi]$. Once equation 2.13 is solved, we will have the *complex mode bispectrum*. However, we are solely interested in visualizing it's modulus, $|\lambda_1(f_k, f_l)|$. This is the *magnitude mode bispectrum* but as we are solely focusing on the modulus, we will simply be referring to it as the mode bispectrum throughout this work.

A necessary discussion now is the use of the spatial homogeneity of the data set as initially mentioned in Chapter 1. As stated previously, we applied the DFT on the data of the DNS of open cavity flow because the three-dimensional data is periodic in the z-direction. Doing so improves computational efficiency, the convergence of the spectral estimate, and interoperability of results [25]. This means that the BMD will be considering triadically consistent wavenumber triplets $\{k_1,\ k_2,\ k_1 + k_2\}$. For our case with spanwise wavenumbers in the z-direction, k_z, the triadically consistent triplets are $\{k_{z_1},\ k_{z_2},\ k_{z_1} + k_{z_2}\}$. The BMD is therefore computed from the discrete-space discrete-time transformed data $\hat{\mathbf{q}}(\mathbf{z}, k, f)$, where we denote the position vector of the remaining inhomogeneous directions by $\mathbf{z} = [x, y]^T$. The bispectral density matrix specializes as,

$$\mathbf{B}(\mathbf{x}, \mathbf{x}', f_k, f_l) \rightarrow \mathbf{B}(\mathbf{z}, \mathbf{z}', k_i, k_j, f_k, f_l), \tag{2.14}$$

and is computed from $\hat{\mathbf{q}}(\mathbf{z}, k_i, f_k)$, $\hat{\mathbf{q}}(\mathbf{z}, k_j, f_l)$, and $\hat{\mathbf{q}}(\mathbf{z}, k_{i+j}, f_{k+l})$. The resulting bispectral modes are two-dimensional and will be two-dimensional for the rest of the analysis.

Now that the bispectral modes and mode bispectrum have been computed using the methods outlined, move on to the summed mode spectrum. Following [25] once more, we define the summed mode spectrum to be,

$$\Lambda_1(f_3) \equiv \frac{1}{N(f_3)} \sum_{f_3=f_1+f_2} |\lambda_1(f_1, f_2)|, \tag{2.15}$$

where $N(f_3)$ is the number of frequency doublets $\{f_1, f_2\}$ that contribute to any frequency $f_3 = f_1 + f_2$. This definition is analogous to the common definition of a summed bispectrum for time signals and is graphically equivalent to summing λ_1 along diagonals of slope -1 (see Figure 3.3 in Chapter 3, section 2). Summing along these diagonals means summing λ_1 values that correspond to a constant frequency in the mode bispectrum.

The above was intended as a summary of the mathematics behind the BMD and greatly followed the process outlined by Schmidt in [25]. For more detail and background, readers are directed to that work. However, there are a few slight differences worth noting. Primarily, the MATLAB code used to compute the BMD, and thus the results in Chapter 3, is not the exact same as the MATLAB code discussed in [25]. Instead, the code used here is a recently published update that is currently available on the MathWorks website [26]. This updated code computes the energy transferred into and out of f_3. Another major difference to note is the option of using Mengi and Overton's [16] algorithm to solve equation 2.13, which was the algorithm we elected to use whenever the BMD was computed. Furthermore, we will be using the *cross*-BMD as we are interested in the cross-correlated inputs: the wavenumber triplets $\{k_{z_1},\ k_{z_2},\ k_{z_1} + k_{z_2}\}$. Nevertheless, we will continue to refer to the decomposition simply as the BMD rather than the cross-BMD.

Mode bispectrums, bispectral modes, and summed mode spectrums have now been defined and computed using the BMD. To sift through the data contained in these plots, we now move on to our second core method of analysis, the radial search algorithm.

2.2 Radial Search

It was decided to search the λ_1 computed by the BMD with a radial search algorithm in order to find local maxima. This radial search algorithm was developed with several functionalities built-in that are intended to provide users not only with quality of life features, but also to aid in their analysis of the results from the BMD. It will be used on the aforementioned mode bispectrum not only to find maxima, but to assist in determining what frequency interactions possibly interesting bispectral modes occur at. Radially searching the mode bispectrum and summed mode spectrum culminates in a new type of visualization we will call the *sparse mode bispectrum*. The intended purpose of the sparse mode bispectrum is to condense the results from radially searching the mode bispectrum and summed mode spectrum into one succinct visualization that summarizes the key results of the BMD.

The output array of the BMD code that makes up the complex mode bispectrum has dimensions $(N_{freq} \times N_{freq})$, where N_{freq} refers to the total number of frequencies. When searching the mode bispectrum λ_1 values, we are interested in the modulus and as such the following is done before beginning the radial search,

$$\log_e |\lambda_1| . \tag{2.16}$$

Each $\log_e |\lambda_1|$ value in the mode bispectrum is compared to neighboring $\log_e |\lambda_1|$ values that fit inside a circle that has a user-defined radius of f_r. In essence, every $\log_e |\lambda_1|$ value that is inside the circle in the mode bispectrum defined by:

$$f_1^2 + f_2^2 \leq f_r^2, \tag{2.17}$$

is compared to the $\log_e |\lambda_1|$ value at the center of this circle. This is analogous to the equation of a circle in a Cartesian coordinate system centered at zero. However, as we are interested in each comparing each $\log_e |\lambda_1|$ value to its neighbor in the mode bispectrum and each occurs at

various frequency components, f_k and f_l, we are therefore rarely centered at $f_k = f_l = 0$. The center is constantly redefined by the frequency triad that corresponds to the $\log_e|\lambda_1|$ currently being compared to its neighbors and as such, the circle that is considered at any one time is more accurately defined by:

$$(f_1 - f_k)^2 + (f_2 - f_l)^2 \leq f_r^2, \tag{2.18}$$

where f_k and f_l correspond to the frequencies of the triad of the current $\log_e|\lambda_1|$ value we are centered about while f_1 and f_2 correspond to the frequencies of the $\log_e|\lambda_1|$ inside the circle. If

$$\log_e|\lambda_1(f_k, f_l)| \geq \log_e|\lambda_1(f)|, \qquad f \in \{(f_1 - f_k)^2 + (f_2 - f_l)^2 \leq f_r^2 |\, f \neq 0\}, \tag{2.19}$$

then the value at the center of this circle is greater than or equal to all other neighboring values and is considered a maxima by the radial search algorithm. Values that satisfy 2.19 are saved along with their corresponding frequencies. If users elect to choose a greater f_r value a larger circle is formed and it is less likely for a maxima to be detected as the centered value is compared to more neighboring values. Figure 2.1 showcases visually how the radial search algorithm works when radially searching the array that makes up the mode bispectrum.

Once the relevant $\log_e|\lambda_1(f_k, f_l)|$ maxima values have been found through radially searching the mode bispectrum, we will analyze the bispectral modes, ϕ_{k+l}, at the same frequencies, f_k and f_l, where these maxima occurred. An accompanying code automates this process and uses the radial search algorithm to arrange these bispectral modes in the relative shape of the mode bispectrum. Bispectral modes are arranged in such a manner so as to give insight to the modes' behavior relative to the mode bispectrum. These bispectral modes will be the last visualization we explore and can be found in Chapter 3, section 4.

The radial search algorithm works not only for arrays with dimensions $(N_{freq} \times N_{freq})$, but also for vectors that are length $(N(f_3) \times 1)$. These are vectors that have a length equal to the number of frequency doublets that contribute to any frequency f_3. This is a necessary function

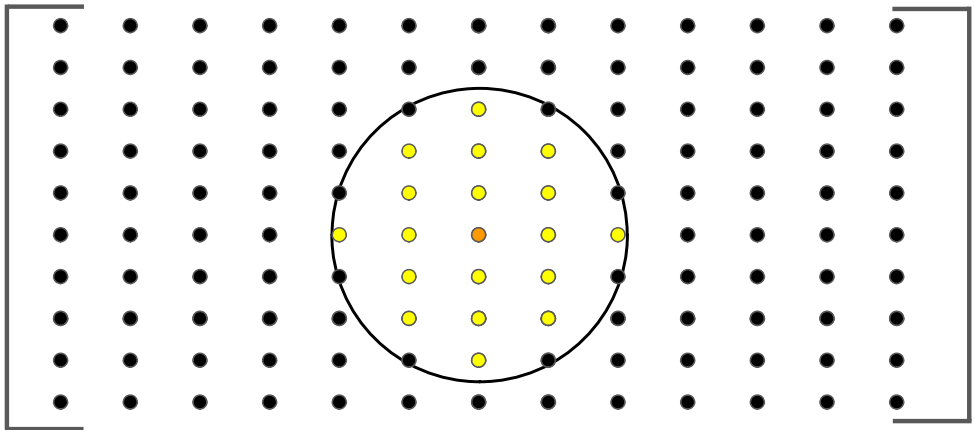

Figure 2.1. Visualization of the radial search algorithm. The center value colored in orange is compared to all values inside the circle defined by equation 2.18, which are colored in yellow. If the orange value is greater or equal to all the yellow values, then it is considered a maxima. Otherwise, it is not considered a maxima and the radial search is re-centered to the next neighboring value where the process is repeated. Values that are not completely inside the circle, such as the 8 black values near the radial search circle, are not considered in the comparison.

for the radial search algorithm because we are interested in also finding the maxima of the summed mode spectrum. As the summed mode spectrum is a *spectrum*, this implies the radial search algorithm has a peak finder capability built-in. The radial search algorithm accomplishes this by comparing $\Lambda_1(f_3)$ values from 2.15 to its neighbors. Like the radial search of the mode bispectrum, we accomplish this by treating one $\Lambda_1(f_3)$ value as a center and compare it to values that correspond to frequencies doublets that are less than or greater than the current frequency f_3. This is equivalent to comparing $\Lambda_1(f_3)$ values that are to the left and to the right of the center at f_3 on a number line. As such, one $\Lambda_1(f_3)$ value at f_3 is compared to its neighbors that are in the interval,

$$f_3 - f_r \leq f \leq f_3 + f_r, \tag{2.20}$$

where $f_3 = f_1 + f_2$ as before. If

$$\Lambda_1(f_3) \geq \Lambda_1(f) \qquad f \in \{\,[f_3 - f_r, f_3 + f_r] \,|\, f \neq f_3\}, \tag{2.21}$$

then $\Lambda_1(f_3)$ is greater than or equal to all other neighboring $\Lambda_1(f)$ values and is considered a

maxima. Like before, the value is saved along with the corresponding frequencies of the triad. An analog to this one dimensional radial search would be a linear search of a number line that is length $2f_r$. Similarly to radially searching the mode bispectrum, increasing f_r makes the search stricter and less likely to consider values maxima as they are being compared to more neighboring values.

Now that we radially searched the mode bispectrum and summed mode spectrum in order to for their respective maxima, we can create the sparse mode spectrum. The sparse mode bispectrum takes inspiration from the visualization of the mode bispectrum found in Moczarski and et al's work [18]. In their work, the mode bispectrum is plotted as a scatter plot with the size and color of points representing $|\lambda_1(f_k, f_l)|$. This scatter plot is accompanied by three dashed lines that are plotted diagonally with slope -1 and represent the frequencies $f = f_1 + f_2$ for the three modes found at $f = \{0, 1, 2\}$.

For the sparse mode bispectrum, however, we will be using the results of the radial search algorithm as its foundation. Visually speaking, the sparse mode bispectrum consists of a scatter plot with colored points that vary in size and dashed diagonal lines of slope -1. The dashed lines contain information from the summed mode spectrum, the color (and intensity) of the points plotted contain information from the energy terms output by the BMD, and the size of the points contain information from the mode bispectrum. We will now go over each aspect of the visualization in more detail.

The dashed lines in the sparse mode bispectrum will correspond to the maxima found from applying the radial search algorithm to the summed mode spectrum. As such, they represent peaks in the summed mode spectrum and are labeled as f_3 in the plot as these frequencies are simply $f_3 = f_1 + f_2$ as defined before. The exact value of $\Lambda_1(f)$ is not represented in the sparse mode bispectrum; we are only concerned with the frequency f_3 these peaks occur at.

The points in the sparse mode bispectrum are the points found by radially searching the mode bispectrum. Only the $\log_e |\lambda_1(f_k, f_l)|$ values which are greater than their neighbors in a circle of radius f_r are considered. These values are *not* what determines the color of the scatter

points. Instead, the frequencies f_k and f_l that correspond to that particular maxima in the mode bispectrum are used to find the corresponding energy terms computed by the BMD which then determine the color of the point. The color of the point represents whether energy was gained into f_3 or lost from f_3. If points are colored blue, energy was lost from f_3. Likewise, points colored red indicate that energy is going into f_3. Points that are simply white circles indicate no loss or gain of energy. The more intense the color the larger in magnitude the energy that has been transferred. For clarity, the range of values and their associated color are represented by a color bar. The color bar has its color range correspond to the absolute maximum energy term computed by the BMD of the entire data set rather than solely to the points that are plotted. This is done so that the sparse mode bispectrum can suggest whether the intensity of energy transferred at the found points of interest are small or large relative to the rest of the mode bispectrum. If the visualization were to consist of exclusively pale blue and red points then that would indicate that the largest energy transferred occurred at a frequency interaction *not* found by the radial search algorithm. The color bar is a gradient from blue to white to red and is a slightly modified version of the code `bluewhitered.m` from Nathan Childress readily available on the MathWorks website [2]. Points in the sparse mode bispectrum are outlined in black for visual clarity; white circles on a white background would be obfuscated greatly.

Lastly, we include the information provided by the $\log_e |\lambda_1(f_k, f_l)|$ values of the mode bispectrum through the *size* of the circles plotted. The smallest maxima are half the size of the largest maxima found in the mode bispectrum. This is done because if the value for $\log_e |\lambda_1(f_k, f_l)|$ is surprisingly small in magnitude then it would be difficult to see the circle in the visualization if no sizing convention was used. Users can easily change this sizing convention. For example, users can elect to use the sizing convention where the smallest maxima in the mode bispectrum is a third of the size of the largest maxima.

Due to the reasons discussed above, the sparse mode bispectrum is able to contain information from the mode bispectrum, the summed mode spectrum, and the energy terms output from the BMD. A few of the quality of life features of the radial search algorithm have not yet

been discussed and are worth mentioning here before showcasing results. By default, the radial search returns all of the maxima found through its search in a list which is then sorted from greatest maxima value to least maxima value. Users may request n maxima and the radial search will instead return the first n maxima from the sorted list. For example, if a user requests $n = 10$ maxima, only the ten largest maxima found by the radial search will be returned. However, this occurs only if there are $> n$ maxima found, otherwise, the radial search will behave like usual and return all maxima found.

Other quality of life features not yet mentioned are visual settings designed with the intent of improving the visual clarity of the visualizations that are produced using the radial search algorithm, such as changing the distance between the bispectral modes when they are arranged in the relative shape of the mode bispectrum. As this discussion has been about *visualizations*, it is best to move onto Chapter 3 to *see* the visualizations and features in practice as discussed throughout this chapter.

Chapter 3

Results and Discussion

Before presenting the final results of our analysis, it is important to note the spectral parameters that were used when computing the BMD as they can affect the end results. The spectral parameters used, along with the appropriate variables, are defined and reported in Table 3.1. The algorithm used to solve equation 2.13 also affects the results of the BMD, and as mentioned in the previous chapter, Mengi and Overton's algorithm was used whenever the BMD was computed. Also, while the spanwise wavenumbers considered are the integers $0 \leq k_z \leq 3$, for the purposes of our primary discussion, we will be focusing on the self-interaction in the spanwise wavenumber triplet $\{0,0,0\}$. Spanwise wavenumber triplets $\{k_{z_1},\, k_{z_2},\, k_{z_1}+k_{z_2} \leq 3\}$ were analyzed with the BMD and radially searched; they can be found in the appendix as additional results.

Finally, our results will be presented with the dimensionless frequency that corresponds to the Strouhal number. However, The notation of f will be maintained for continued readability. We will explicitly note whenever this distinction affects our analysis.

Table 3.1. The spectral parameters used for the BMD. N_t denotes the number of snapshots, N_{fft} denotes the number of fast Fourier transformations, N_{ovlp} denotes the number of overlap between blocks, N_{blks} denotes the number of blocks, and tol denotes the tolerance used by the algorithm to solve equation 2.13. The variables u, v, and w refer to the streamwise, transverse, and spanwise velocities, respectively. Variable T denotes the temperature and ρ denotes the density. All the variables have a $\hat{}$ above them due to the use of the DFT in the z-direction.

Variables	N_t	Δt	N_{fft}	N_{ovlp}	N_{blks}	tol
$\hat{u}\ \hat{v}\ \hat{w}\ \hat{T}\ \hat{\rho}$	5000	0.25	256	128	38	10^{-8}

3.1 Mode Bispectrum

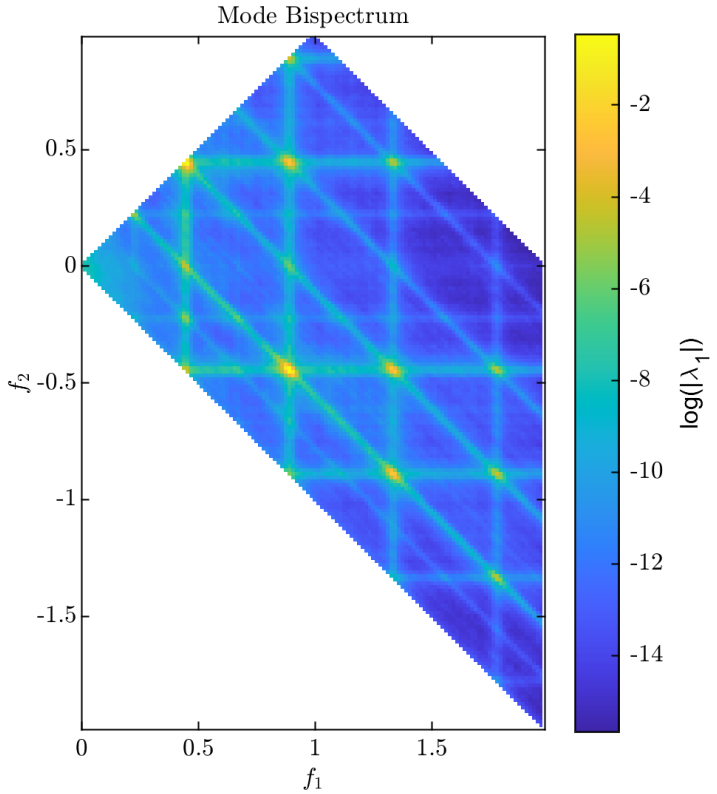

Figure 3.1. Mode bispectrum for spanwise wavenumber triplet $\{0,0,0\}$. The x-axis corresponds to frequencies f_1 while the y-axis corresponds to frequencies f_2. The color bar indicates the value of $\log_e |\lambda_1|$.

Figure 3.1 showcases the mode bispectrum for the spanwise wavenumber triplet $\{0,0,0\}$. Values that correspond to $(f_1,0,f_1)$, i.e. values parallel to the x-axis at $f_2 = 0$, correspond to the

intrinsic dynamics of the flow and are where unstable global modes would appear. Triads of the form $\{f_1, f_2 = -f_1, 0\}$ correspond to non-linear interactions of the mean flow deformation, while harmonic interactions correspond to triads of the form $\{f_1, f_1, 2f_1\}$. What's particularly interesting about this mode bispectrum is its grid-like pattern appears to have maxima which are easy to pick out visually. Consequently, this mode bispectrum helps verify the validity of our radial search algorithm. We elect to use a radial search frequency of $f_r = 0.2$ as it will produce a radial search circle that is large enough- and thus *restrictive* enough- to pick out relevant $\log_e |\lambda_1|$ values. The search radius is something for users to define and can be determined through trial-and-error (as done here) or through other satisfying means. Applying the radial search to the mode bispectrum in Figure 3.1 produces Figure 3.2.

A radial search with f_r on the mode bispectrum as shown in Figure 3.2 results in a total of 28 maxima found. The f_r we chose to search with has proven to be restrictive enough to find the maxima we were initially interested in. If we are interested in finding the frequency f_3 these maxima occur at we simply have to add the values represented by (f_1, f_2) as $f_3 = f_1 + f_2$. We elect now to utilize the radial search algorithm's feature to report the $n = 10$ largest maxima. This does not produce a distinctive visual change compared to Figure 3.2; the only difference is there would be 10 maxima labeled rather than the current 28. As such, we do not re-plot the figure and instead report the exact values in Table 3.2 which can then be compared to those labeled in Figure 3.2.

As shown in Table 3.2, only one global mode is considered to be in the top ten maxima and it is the ninth largest local maxima; the global mode that occurs at $f_1 = 0.44$. As this is the only global mode we found, we label it as $f_0 = 0.44$ and quickly see that the other nine maxima are all harmonic combinations of this frequency. We see from Table 3.2 that the global maxima has the triad $\{2f_0, -f_0, f_0\}$, the second largest maxima is $\{f_0, f_0, 2f_0\}$, the third largest maxima is $\{3f_0, -f_0, 2f_0\}$, and so on. Each of the top ten maxima found with the radial search is some harmonic sum or difference interaction with the frequency $f_0 = 0.44$, which itself appears to be an unstable global mode. The eighth largest maxima caused by the triad $\{f_0, -f_0, 0\}$

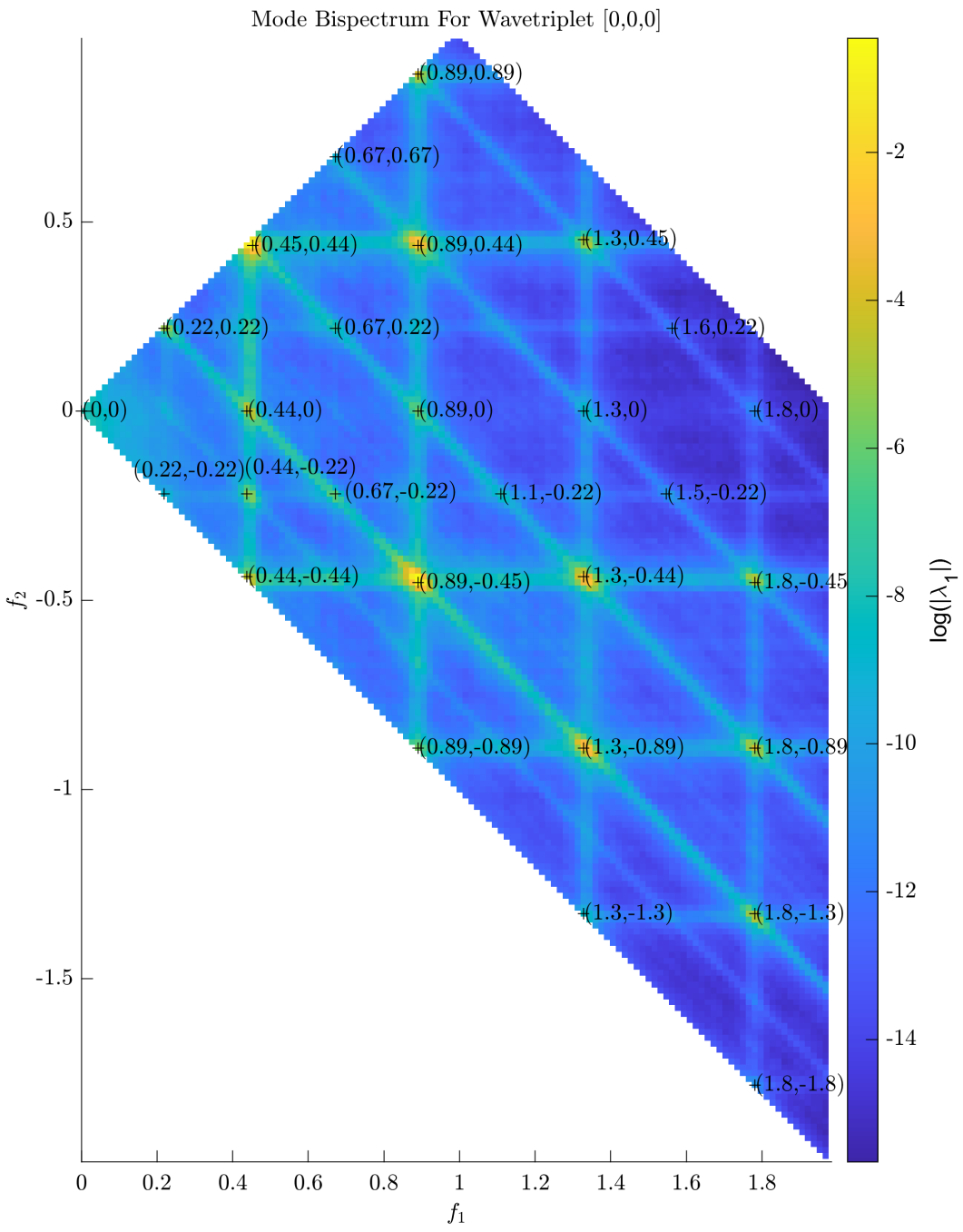

Figure 3.2. Mode bispectrum for spanwise wavenumber triplet $\{0,0,0\}$ after a radial search of $f_r = 0.2$ is applied. The locations with a maxima are marked with a $+$ symbol. Accompanying these points are coordinates in the form (f_1, f_2). The mode bispectrum has been enlarged for visual clarity and legibility of coordinates.

Table 3.2. Top ten maxima of the mode bispectrum for spanwise wavenumber triplet $\{0,0,0\}$ along with the frequencies f_1, f_2 and f_3 they occur.

f_1	f_2	f_3	$\log_e \lvert\lambda_1\rvert$
0.89	−0.45	0.44	−0.457
0.45	0.44	0.89	−0.479
1.33	−0.44	0.89	−2.488
1.33	−0.89	0.44	−2.552
0.89	0.44	1.33	−2.562
1.78	−0.89	0.89	−4.032
0.89	0.89	1.78	−4.036
0.44	−0.44	0.00	−4.502
0.44	0.00	0.44	−4.519
1.78	−1.33	0.45	−4.775

indicates a difference-interaction of the fundamental instability with itself that leads to a mean flow deformation. This means that the mode bispectrum detected a non-linear self-interaction that generated a mean flow deformation, with the radial search algorithm confirming this interaction as one of the 10 largest in the entire bispectrum. It is worth noting the frequency harmonic values differ ± 0.01 from being exactly nf_0 (where n is an integer). This discrepancy is due to rounding errors and is insignificant to the conclusions drawn.

With these initial results of the BMD and radial search algorithm, we now turn to the summed mode spectrum as it is a proxy for the frequency interactions that are expected to have the largest energy transfers and will therefore bring more insight into this flow.

3.2 Summed Mode Spectrum

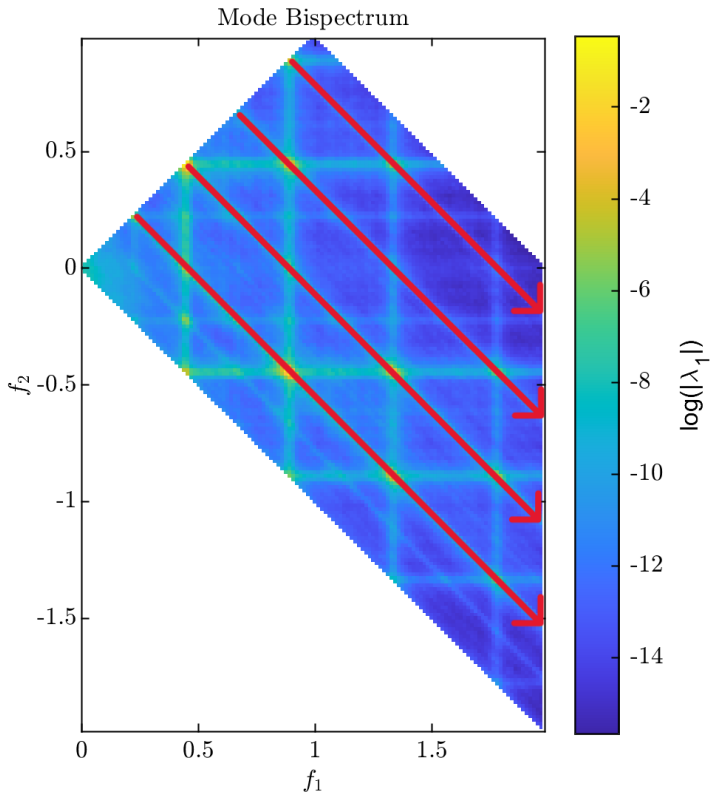

Figure 3.3. Mode bispectrum for spanwise wavenumber triplet $\{0,0,0\}$ with 4 lines of slope -1 highlighted. Each diagonal line corresponds to a (unique) constant $f_3 = f_1 + f_2$. There are more f_3 than indicated by the four diagonal lines; this depiction is for emphasis on the relationship between the mode bispectrum and the summed mode spectrum.

As mentioned in Chapter 2, section 1, the summed mode spectrum is defined from the BMD with equation 2.15. Graphically, this is equivalent to summing values along a slope of -1 as shown in Figure 3.3. Computing the necessary values by summing along all diagonals of constant f_3 gives us Figure 3.4, the summed mode spectrum for spanwise wavenumber triplet $\{0,0,0\}$. Immediately, one can see several peaks in the spectrum. To identify the ones we believe to be worth analyzing, we apply the radial search algorithm in one-dimension (a misnomer discussed in Chapter 2, section 2) with $f_r = 0.2$ to keep the results consistent with what was found previously. Doing so gives us the accompanying summed mode spectrum found in Figure 3.5. Peaks in

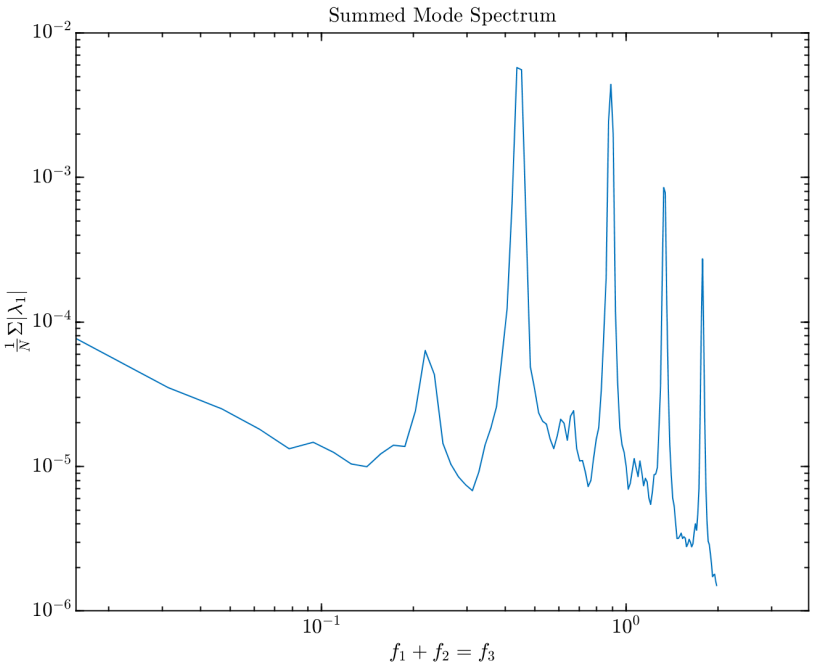

Figure 3.4. Summed mode spectrum for spanwise wavenumber triplet $\{0,0,0\}$. Each f_3 corresponds to a diagonal line of slope -1 in the mode bispectrum. Note: both axes are in log scale.

the summed mode spectrum correspond to frequencies that are involved in quadratic non-linear interactions but without discerning between the contributing triads.

A total of five maxima were found in the summed mode spectrum using this process. Unfortunately, the maxima at $f_3 = 0$ is not labeled in either of the two above figures due to plotting in $\log - \log$ scale. This is something that is rectified in the sparse mode bispectrum visualizations as we will see in the next section.

Nevertheless, though the radial search found 28 maxima in the mode bispectrum, only five were found in the summed mode spectrum. Several maxima in the mode bispectrum are along the same diagonal meaning they contribute to the same f_3 frequency. As such, there will necessarily be fewer maxima in the summed mode spectrum than the mode bispectrum. Notably, the radial search algorithm did not consider the peak at $f_3 = 0.22$ relevant. As our chosen f_r is 0.2, both peaks at $f_3 = 0.22$ and $f_3 = 0.42$ would be compared. Clearly shown by the two figures, $f_3 = 0.42$ has a larger value so $f_3 = 0.22$ is not considered a maxima. The five

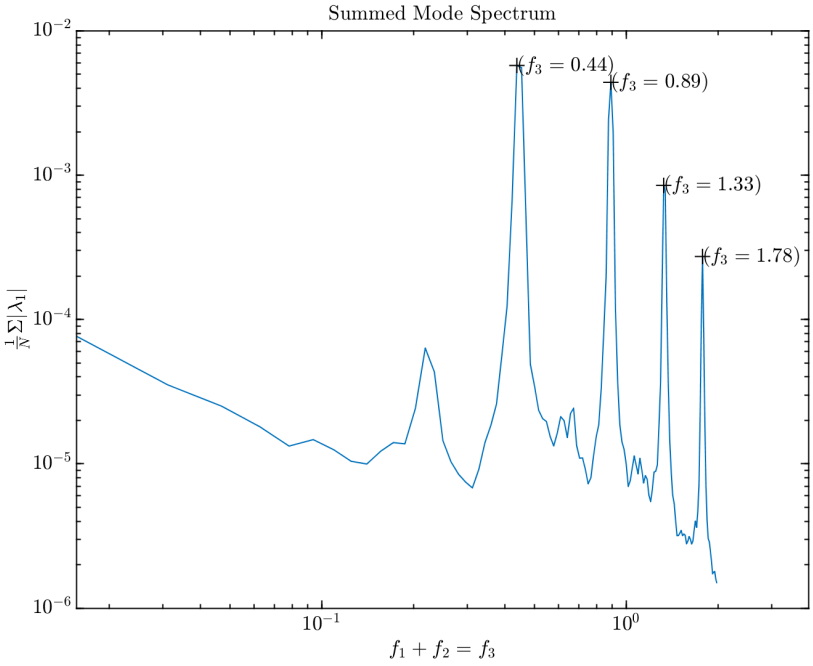

Figure 3.5. Summed mode spectrum for spanwise wavenumber triplet $\{0,0,0\}$ after a radial search of $f_r = 0.2$ is applied.

values found with the one-dimensional radial search are reported in Table 3.3. Interestingly, excluding repeating results, the order of the frequencies, f_3, that correspond to the maxima found in the mode bispectrum in Table 3.2, are in the same order as those found in the summed mode spectrum shown in Table 3.3. This indicates that the maxima found in the mode bispectrum have a significant impact on the maxima found in the summed mode spectrum.

Furthermore, the peaks in the summed mode spectrum are a proxy for the frequency interactions that are expected to have the largest energy transfers and are therefore expected to

Table 3.3. The five maxima of the summed mode spectrum for spanwise wavenumber triplet $\{0,0,0\}$ ordered from greatest to least $\Lambda_1(f_3)$ value.

f_3	$\Lambda_1(f_3)$
0.44	0.0058
0.89	0.0044
1.33	0.00085
1.78	0.00027
0.00	0.00013

be the Rossiter modes of the open cavity flow. As mentioned in Chapter 1, section 2, Rossiter modes correspond to large-amplitude, self-sustained oscillations of the pressure, velocity, and density fields in and around the cavity [9]. Utilizing equation 1.4, we can empirically compute the frequencies where these modes are expected to occur and compare with the results of the summed mode spectrum. As we are using the dimensionless frequency corresponding to the Strouhal number as noted at the beginning of this chapter, the equation will be slightly different. The equation is now,

$$f = \frac{m - \gamma}{\frac{1}{K} + Ma}, \tag{3.1}$$

to keep inline with the definition of the Strouhal number, $St = \frac{fL}{U}$. The definitions of each variable is the same as before in equation 1.4. Again, we will continue to use f to refer to the dimensionless frequency for readability. The frequencies obtained are presented in Table 3.4.

Table 3.4. Rossiter mode frequencies according to equation 1.4. Only the first four are presented as the largest frequency computed from the BMD parameters is $f = 2$ and Rossiter mode five would occur beyond $f = 2$.

Rossiter mode, m	f
1	0.33
2	0.78
3	1.22
4	1.66

By comparing the non-zero f_3 values found in Table 3.3 with the frequencies f found in Table 3.4, we see that Rossiter modes were predicted to occur at lower frequencies. In general, they were predicted to occur at $\approx f_3 - 0.11$ rather than what was obtained using the BMD. The peak at $f_3 = 0$ found by the radial search algorithm is not indicative of a Rossiter mode, but rather, the frequency interactions that correspond to the mean flow deformation of the flow. This means that the values reported in Table 3.2 are more specifically non-linear triadic interactions resulting in the Rossiter mode frequencies for this flow. The peak seen at $f_3 = 0.22$ but not detected by the radial search algorithm in the summed mode spectrum is not believed to be a

Rossiter mode. Rossiter modes often have comparable strength [9] [22]; this peak is noticeably lower in magnitude when compared to the other four. Additionally, the empirical equation 1.4 predicted Rossiter modes occurring at frequencies lower than the ones found in the summed mode spectrum, not higher. Nevertheless, as the peaks in the summed mode spectrum are frequency interactions that are expected to have the largest energy transfers, we will create a sparse mode bispectrum (and summed mode spectrum) with a radial search frequency of $f_r = 0.15$ in the next section to confirm whether or not this is true for the peak at $f_3 = 0.22$. For now, we conclude that the interactions presented in Table 3.2 are actually sum and difference interactions of Rossiter modes, with the difference interaction between the second Rossiter mode and the first leading to the global maxima found in the mode bispectrum.

Now that both the mode bispectrum and summed mode spectrum have been computed and analyzed with the radial search algorithm, we move on to the sparse mode bispectrum.

3.3 Sparse Mode Bispectrum

The sparse mode bispectrum aims to condense all of the relevant information and results obtained from radially searching the mode bispectrum and the summed mode spectrum. Figure 3.6 presents the visualization for the spanwise wavenumber triplet $\{0,0,0\}$. The same 28 maxima found in Figure 3.2 are now colored with respect to their corresponding energy transfer value. Clearly, most of the maxima found in the mode bispectrum do not gain or lose energy; a majority of the points in Figure 3.6 are simply white indicating little-to-no energy transfer. The few colored points are blue and indicate energy being from f_3, with the two largest occurring at $f_3 = 0.44$ and $f_3 = 0.89$.

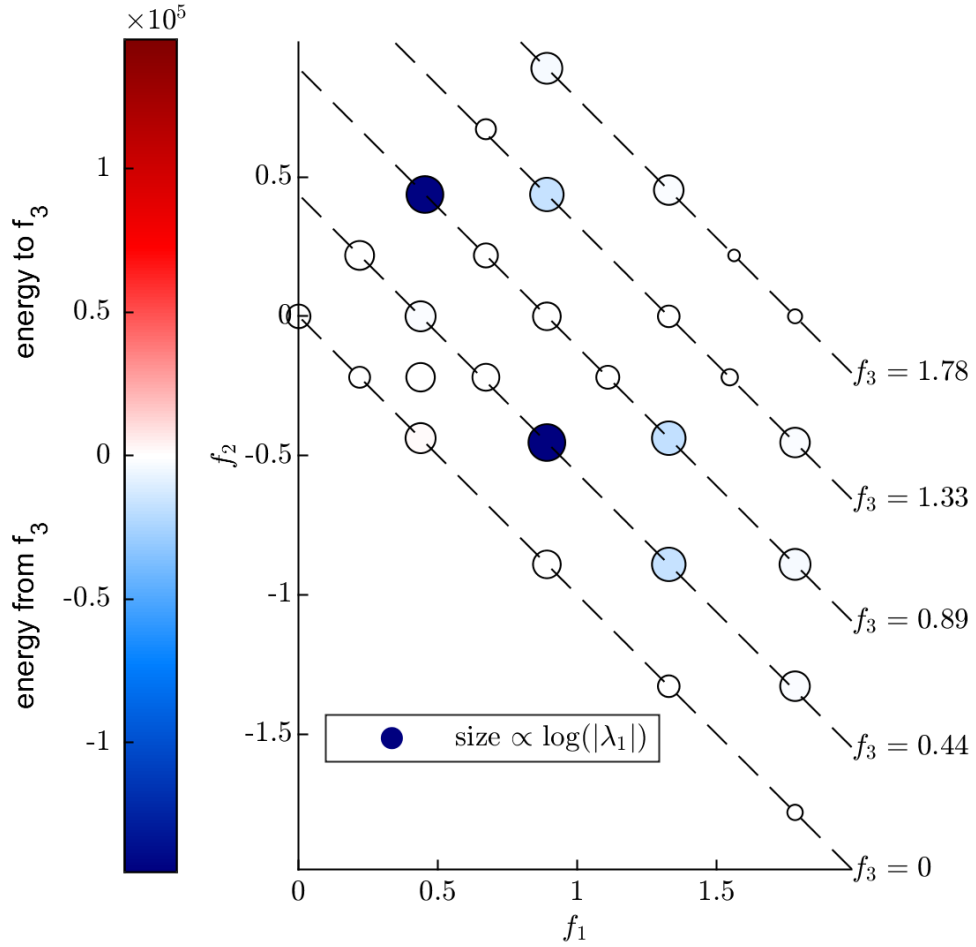

Figure 3.6. Sparse mode bispectrum for spanwise wavenumber triplet $\{0,0,0\}$ after a radial search of $f_r = 0.2$ is applied. Recall, each dashed line f_3 corresponds to a maxima found in the summed mode spectrum and are diagonal lines of slope -1 in the mode bispectrum.

Using the radial search algorithm to report only the top ten values and the ability to re-scale the circles for visual clarity, we obtain Figure 3.7, meaning we now exclusively see the values reported in Table 3.2 in the sparse mode bispectrum. Re-scaling the circles makes it easier to compare the relative $\log_e|\lambda_1|$ values as they are only represented through the size of the circles and appeared to be close in Figure 3.6. In fact, the lighter blue circles in Figure 3.6 appear so close in size to the dark blue circles one may come to the erroneous conclusion that they have the same $\log_e|\lambda_1|$ value in the mode bispecturm. As mentioned in Chapter 2, section 2, the sizes of the circle are relative and it is up to users to determine what scaling (if any) is

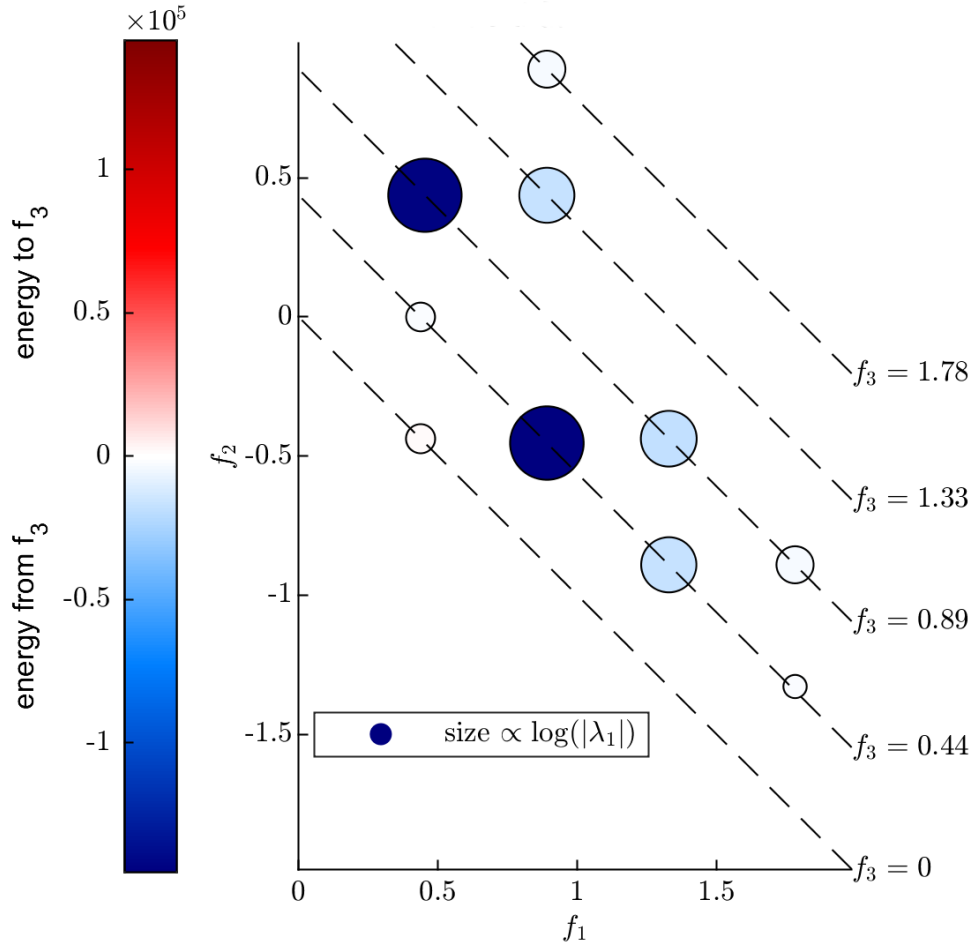

Figure 3.7. Sparse mode bispectrum for spanwise wavenumber triplet $\{0,0,0\}$ with only the top ten values after a radial search of $f_r = 0.2$ is applied. All circles have been scaled by a factor of 4 for improved visual clarity meaning the smallest circles are now $\frac{1}{8}$th the size of the largest circle.

necessary for their visualization.

For our sparse mode bispectrum, after re-scaling, it is clear that the two largest $\log_e|\lambda_1|$ values are also responsible for the largest energy loss from f_3. Furthermore, the local maxima found by radial search algorithm correspond to the largest energy transfers. For this particular flow, all dashed lines- with the exception of the dashed line for $f_3 = 0$- correspond to the Rossiter modes discussed in the previous section. The dashed line for $f_3 = 0$ corresponds to the mean flow deformation and interestingly, does not have any notable energy transfer terms. The first and second Rossiter modes are responsible for the largest energy transfer, with the energy being transferred *from* f_3 rather than *to* f_3. The third Rossiter mode also has an appreciable energy transfer, but it is noticeably smaller than the energy transferred by the first two Rossiter modes. By the fourth Rossiter mode, there appears to be no notable energy transfer. This indicates that the energy being transferred is primarily in the first two Rossiter modes at $f = 0.44$ and $f = 0.89$ with diminishing effects. Due to the sparse mode bispectrum having the same axis convention as the mode bispectrum, we can conclude that no notable energy transfer occurred in the intrinsic dynamics as seen by the white circles parallel to the x-axis at $f_2 = 0$ in Figure 3.6.

Currently, it appears there is a relationship between the largest energy transfers and the peaks corresponding to the Rossiter modes found in the summed mode spectrum. However, as noted previously while analyzing the results in Figure 3.4, there appears to be one more peak at $f_3 = 0.22$ that was not detected by the radial search algorithm due to the search parameter being too strict. This peak is not a Rossiter mode, yet it is possible that triadic interactions resulting in the subharmonic frequency of the first Rossiter mode may also be responsible for energy transfer in this flow. To determine if this is true, we elect to use a less strict radial search frequency of $f_r = 0.15$ and reproduce the summed mode spectrum (Figure 3.8) and sparse mode bispectrum (Figure 3.9). Two more peaks are found in the summed mode spectrum, $f_3 = 0.22$ and $f_3 = 0.67$. The first peak corresponds to the subharmonic frequency of the first Rossiter mode while the second corresponds to the ultraharmonic frequency (with some slight rounding error). The second peak is part of an interesting double peak behavior not originally noted in the

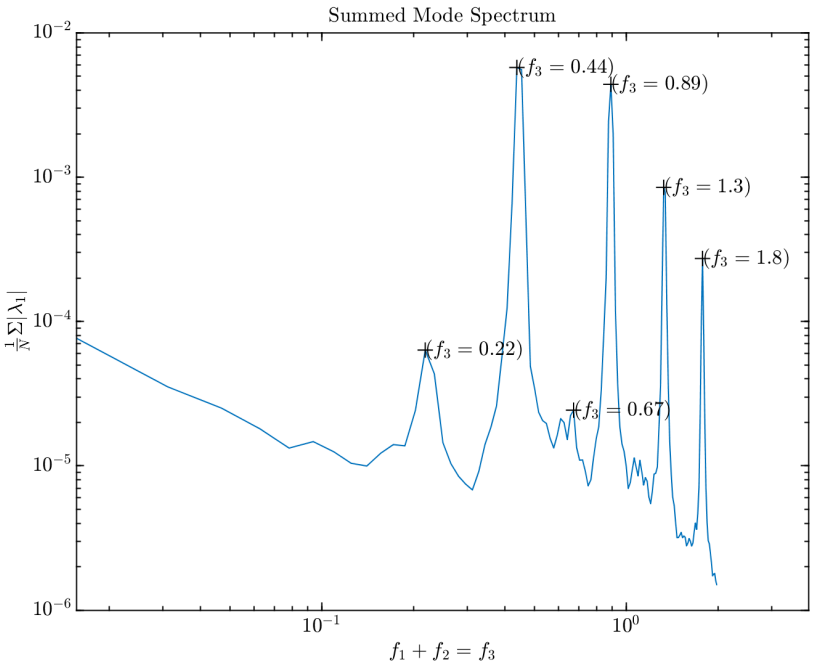

Figure 3.8. Summed mode spectrum for spanwise wavenumber triplet $\{0,0,0\}$ after a radial search with $f_r = 0.15$ is applied.

summed mode spectrum, but besides this, both new peaks are shown to have no notable energy transfer terms. The top ten values of Figure 3.9 are not constructed into a new visualization as this would simply result in Figure 3.7 again.

Through this exercise, we can see that the sparse mode bispectrum is able to condense a majority of the information from radially searching both the mode bispectrum and summed mode spectrum. The Rossiter modes were displayed as dashed lines occurring at frequencies greater than zero, with the dashed line at $f_3 = 0$ corresponding to the mean flow deformation. A second sparse mode bispectrum was produced using a less restrictive radial search frequency, but together, these two visualizations seem to imply that only the largest local maxima in the mode bispectrum are responsible for the energy transferred for the spanwise wavenumber triplet $0,0,0$. The largest maxima found are the non-linear triadic interactions resulting in the Rossiter modes of the open cavity flow, with the first and second modes being responsible for the largest energy transfers. As before, the choice of f_r is left to users to determine in a manner they deem acceptable or useful to their analysis and is easily modified by the radial search algorithm as

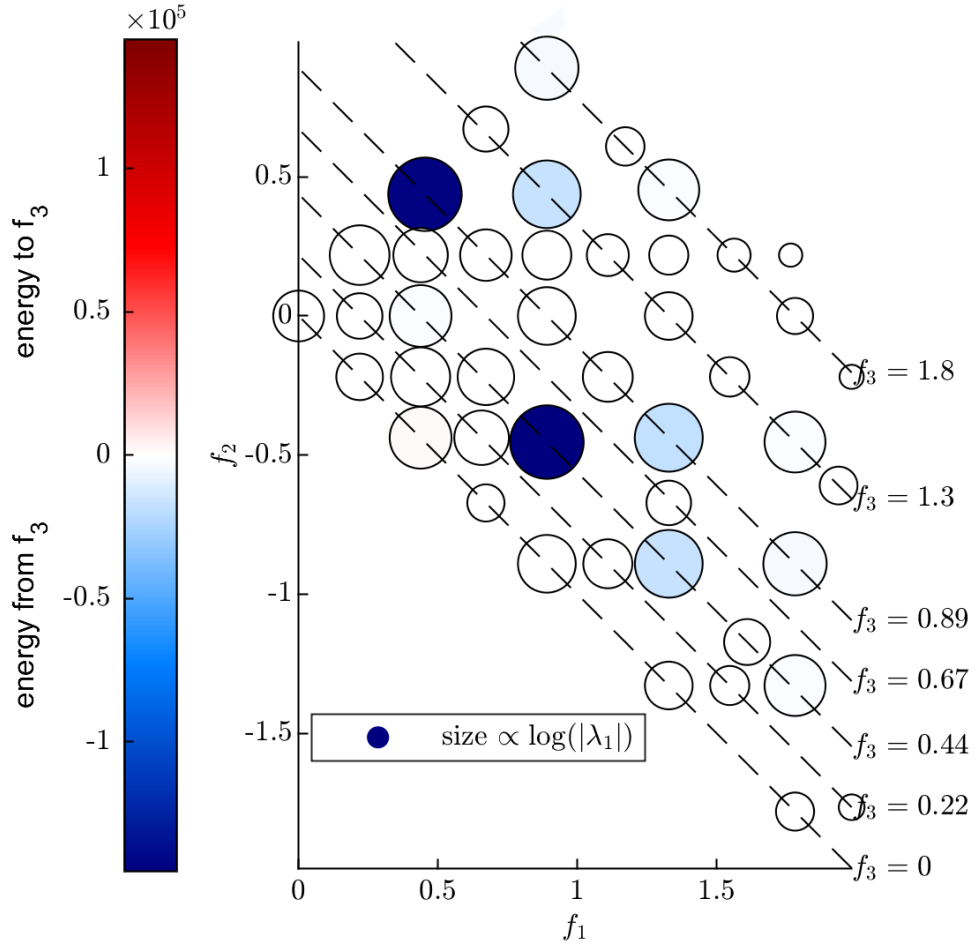

Figure 3.9. Sparse mode bispectrum for spanwise wavenumber triplet $\{0,0,0\}$ after a radial search of $f_r = 0.15$ is applied. All circles have been scaled by a factor of 4 again.

shown between Figure 3.7 and Figure 3.9. We now move onto our final visualization for this data, the bispectral modes arranged in the shape of its respective mode bispectrum.

3.4 Bispectral Modes

The bispectral modes, ϕ_{k+l}, are flow structures that form due to non-linear triadic interactions in the numerical data. They are arranged here in the relative shape of the mode bispectrum so as to showcase these flow structures while maintaining the context of where they occurred in the mode bispectrum. The information gained from radially searching the summed mode spectrum, as well as the information presented in the sparse mode bispectrum, are not necessary for this visualization's formation. Rather, only the results of radially searching the mode bispectrum are required. As the information presented in the sparse mode bispectrum summarizes results from the mode bispectrum and summed mode spectrum, it is intended as a companion to this bispectral mode visualization. We will be plotting the two-dimensional bispectral modes of the streamwise velocity, $\hat{u}$. Figure 3.10 showcases the 28 bispectral modes found when radially searching with $f_r = 0.2$. These bispectral modes correspond to the maxima found in the mode bispectrum as seen originally in Figure 3.2.

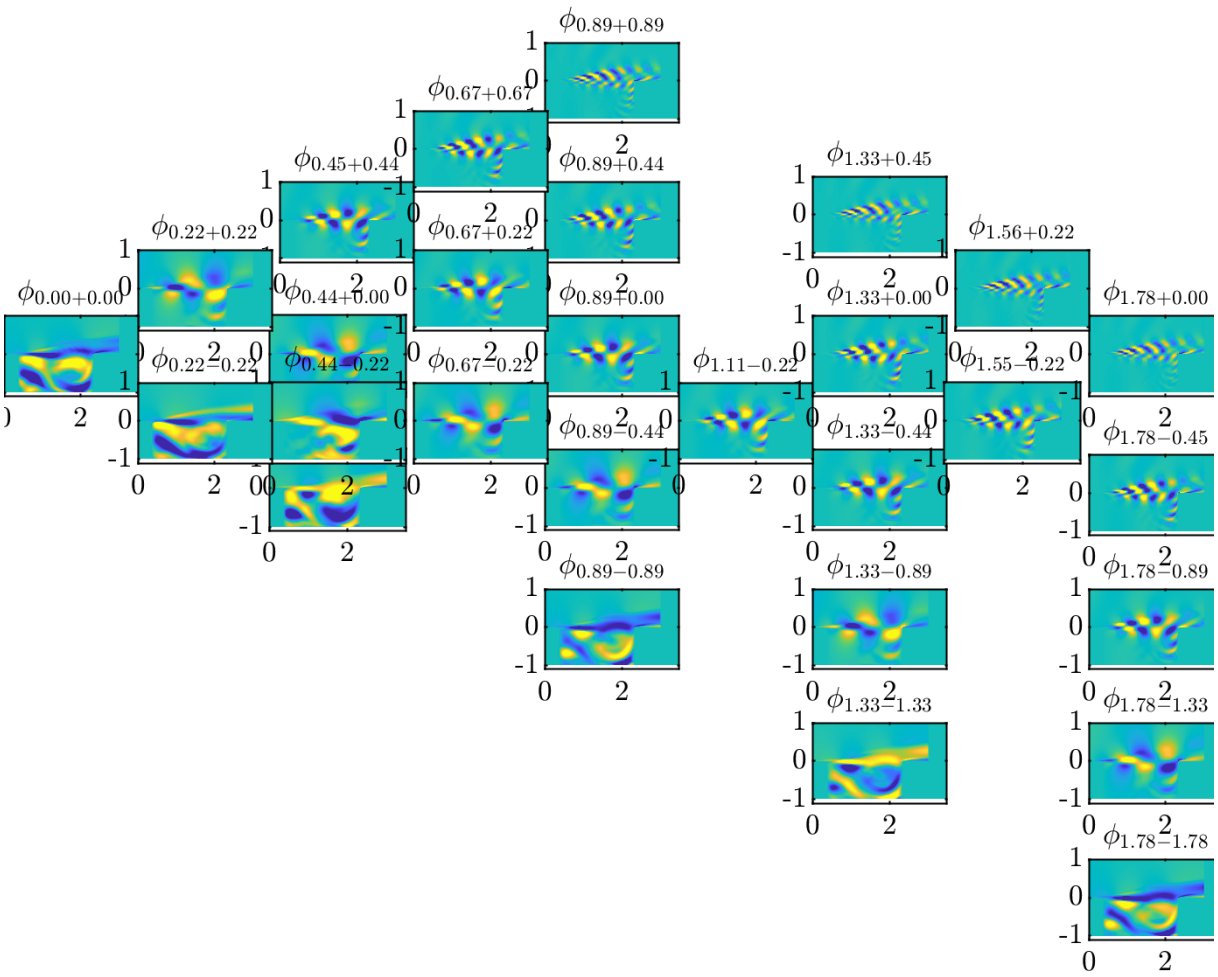

Figure 3.10. Bispectral modes for spanwise wavenumber triplet $\{0,0,0\}$ in the relative shape of the mode bispectrum. The top of each figure is written as $\phi_{f_1+f_2}$.

Figure 3.10 is incredibly busy with all 28 bispectral modes. Several of the smaller inset figures overlap with each other, making the visualization messy and difficult to read. As such, Figure 3.10 is a perfect example as to why one would utilize the radial search algorithm's feature to select only the top n maxima. Choosing $n = 10$ maxima as before and changing the sizes of the inset figures to remove as much overlap as possible produces Figure 3.11.

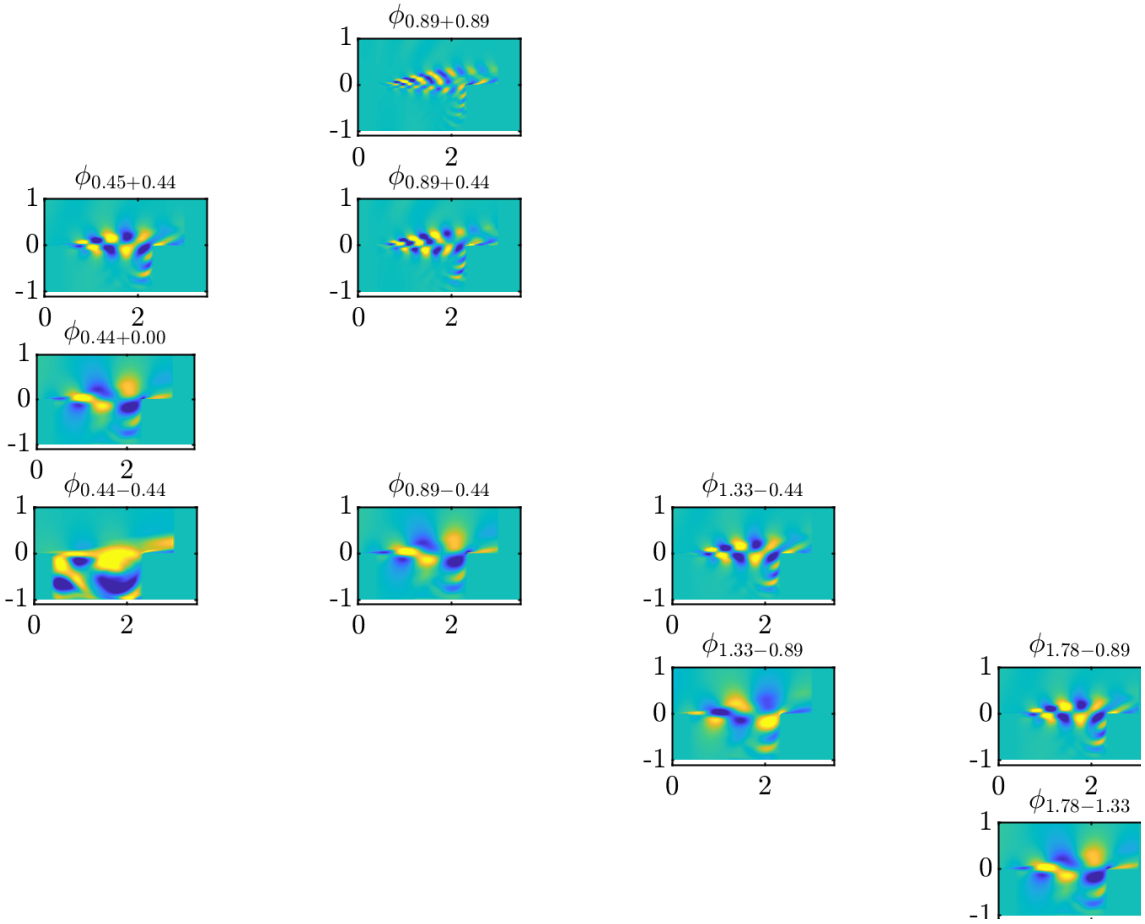

Figure 3.11. Bispectral modes for spanwise wavenumber triplet $\{0,0,0\}$ arranged in the relative shape of the mode bispectrum for the top ten maxima in the mode bispectrum.

In Figure 3.11, we see that the bispectral modes across a diagonal- and thus in the f_3 direction- appear extremely similar. In fact, the diagonal of $f_3 = 0.44$ which consists of $\phi_{0.44+0.00}$, $\phi_{0.89-0.44}$, $\phi_{1.33-0.89}$, and $\phi_{1.78-1.33}$ have similar behavior except for $\phi_{1.33-0.89}$'s inverted colors, implying the values are negatives (and thus occurring in the opposite direction) of the other three bispectral modes. This behavior does not appear to have an easily discernible pattern. Nonetheless, behaviors such as these are much easier to notice due to the the visualization's organization; the information and characteristics behind the mode bispectrum are kept when the bispectral modes are arranged in its relative shape.

Conclusion

In this work, we utilized the BMD on DNS data of open cavity flow after moving to wavenumber space due to the periodicity present in the domain. The BMD extracted flow structures that are associated with triadic interactions and energy transfers in the numerical data. From there, we produced the mode bispectrum, summed mode spectrum, and bispectral modes. To determine where interesting phenomena may be occurring, we utilized a radial search algorithm on the aforementioned results with a frequency search radius of $f_r = 0.2$. Doing so led to 28 maxima identified in the mode bispectrum and five maxima in the summed mode spectrum. We condensed the information from the radial search, mode bispectrum, summed mode spectrum, and energy transfers from the BMD into one concise visualization named the *sparse mode bispectrum*. Using this visualization, we conclude that the largest energy transfer for the spanwise wavetriplet $\{0,0,0\}$ occurs at the two largest maxima found radially searching the mode bispectrum and occur at frequencies $f_3 = 0.44$ and $f_3 = 0.89$. These peaks were found to also be the two largest values in the summed mode spectrum according to the same radial search strictness and are the first two Rossiter modes of the open cavity flow. The 10 largest maxima found by the radial search algorithm were all non-linear triadic interactions resulting in the Rossiter mode frequencies of the open cavity flow, with the exception for the ninth largest maxima. The ninth largest maxima was found to be the first Rossiter mode and corresponds to an unstable global mode as it was found as part of the flow's intrinsic dynamics.

Moving from the sparse mode bispectrum, we plotted the bispectral modes that corresponded to the 28 maxima found in the mode bispectrum. The resulting visualization was crowded with excessive overlap, though the general shape of the bispectral modes were visible.

Focusing on the top ten maxima instead led to a much clearer image and led us to see a general pattern between the bispectral modes: along a constant diagonal of f_3 they appeared to be visually the same. However, we found one bispectral mode to have inverted values, namely the mode $\phi_{1.33-0.89}$, indicating that this mode has the inverse behavior compared to the modes along the same diagonal. This only refers to a change in phase and is not a significant physical phenomena. However, this example has illustrated the key advantage of arranging bispectral modes in the relative shape of the mode bispectrum; information from the mode bispectrum's structure is not lost.

In the future, we could continue to analyze this data set and focus more on the physical phenomena involved rather than succinct visualizations of the BMD. For example, there appeared to be a peak at $f_r = 0.22$ in the summed mode spectrum for this flow which be the subharmonic of the unstable global mode: the first Rossiter mode. However, producing a sparse mode bispectrum with a radial search frequency of $f_r = 0.15$ showed no notable energy transfer terms in this peak or the peak at $f_3 = 0.67$. While the additional results found in the appendix do provide a bit more insight into the flow, questions remain regarding the double peaks found in the summed and the relationship between the Rossiter modes and energy transfer.

Furthermore, We could utilize other analytical and decomposition techniques, such as the aforementioned POD and DMD in Chapter 1, and compare with the results presented here. Insight into the relevance of this peak and the double peak behavior of the spectrum may be obtained. Furthermore, doing so would lead to comparisons the advantages and disadvantages of applying a radial search to the BMD versus other contemporary methods of analysis.

Finally, we could take the approach described in this work and apply it to other data sets that have more interesting and complex mode bispectrums. Mode bispectrums without clear-cut maxima, such as those easily discernible (visually speaking) in Figure 3.1, will likely showcase the advantages of applying a radial search to the results of the BMD in the first place. Phenomena that may have been missed would instead be detected through the concise visualizations presented in this work.

Appendix A

Additional Results

In this section, the mode bispectrum, summed mode spectrum, sparse mode bispectrum, and bispectral modes are presented for $\{k_{z_1},\, k_{z_2},\, k_{z_1}+k_{z_2} \leq 3\}$ spanwise wavenumber triplets. The spectral parameters used to compute the BMD are the same as those reported in Table 3.1. The radial search frequency used is $f_r = 0.2$ as no notable energy transfer terms were found in the sparse mode bispectrum whenever a peak at $f_3 = 0.22$ was found in the summed mode spectrum. The sparse mode bispectrum has the same sizing scaling (a factor of 4) as in Figure 3.7. The bispectral modes were found to always have at least one inverse variation occur along a diagonal, but no discernible pattern was found. In general, all mode bispectrums presented in the appendix appear to have notable spectral leakage along the f_3 direction (diagonal lines of slope -1). For information as to how these visualizations should be interpreted, refer to Chapters 2 and 3.

A.1 Spanwise Wavenumber Triplet $\{k_{z_1},\, k_{z_2},\, k_{z_1}+k_{z_2}=1\}$

This section contains all spanwise wavenumber triplets where $k_{z_1}+k_{z_2}=1$, which consists of only $\{0,1,1\}$. The peaks detected by the radial search algorithm in the summed mode spectrum shown in Figure A.2 are the same peaks as detected in Figure 3.5. Notably, this summed mode spectrum is an order of magnitude weaker compared to the spectrum for $\{0,0,0\}$. Double peaks can be found in the summed mode spectrum between Rossiter modes

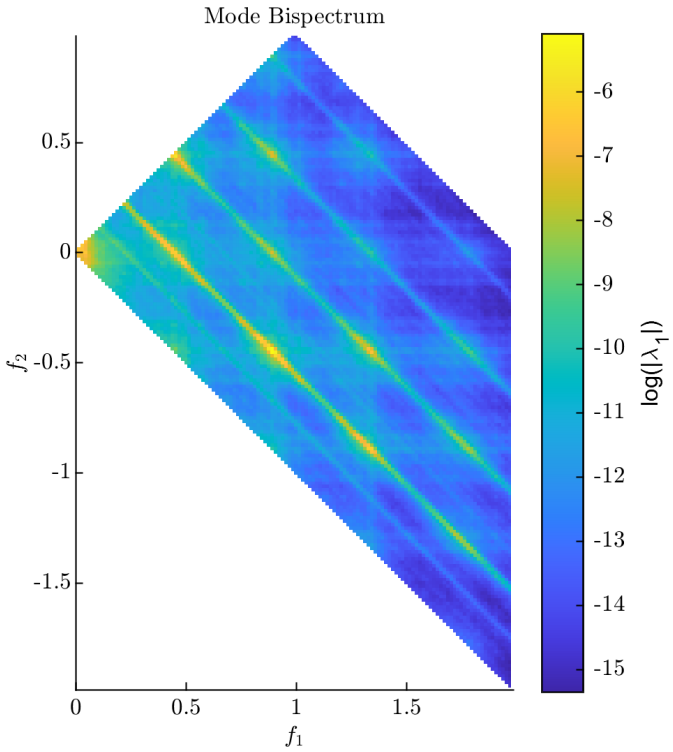

Figure A.1. Mode bispectrum for spanwise wavenumber triplet $\{0,1,1\}$.

and a peak can be seen at $f_3 = 0.22$. Both energy transfer into and from f_3 can be found in this spanwise wavenumber triplet, with the energy into f_3 being greater in the Rossiter modes and the energy from f_3 being greater in the mean flow deformation. Figure A.3 shows notable energy transfer terms in the mean flow deformation, a behavior that was not present for the spanwise wavenumber triplet $\{0,0,0\}$. Once again, the largest energy transfers occur at the largest local maxima, with the magnitude decreasing as the Rossiter mode increases.

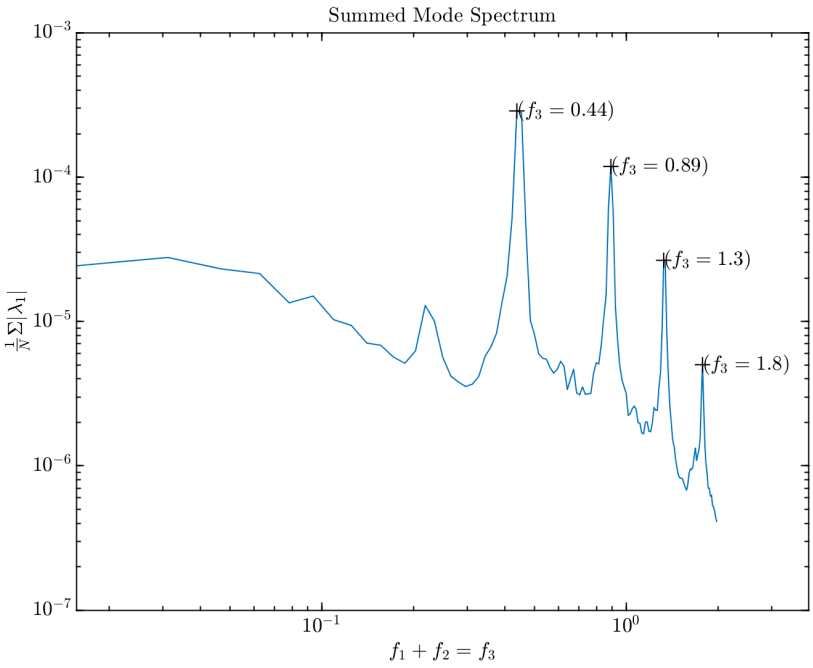

Figure A.2. Summed mode spectrum for spanwise wavenumber triplet $\{0, 1, 1\}$.

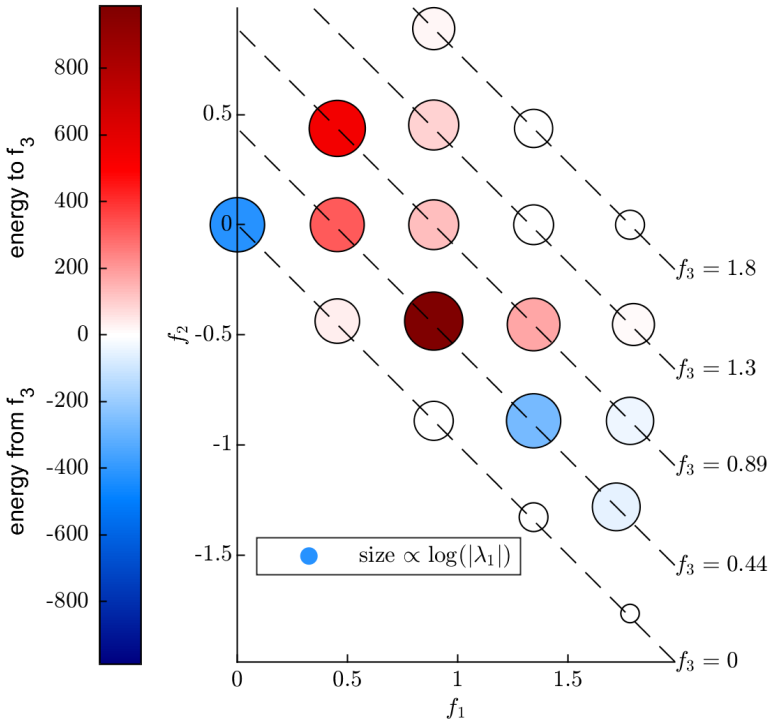

Figure A.3. Sparse mode bispectrum for spanwise wavenumber triplet $\{0, 1, 1\}$.

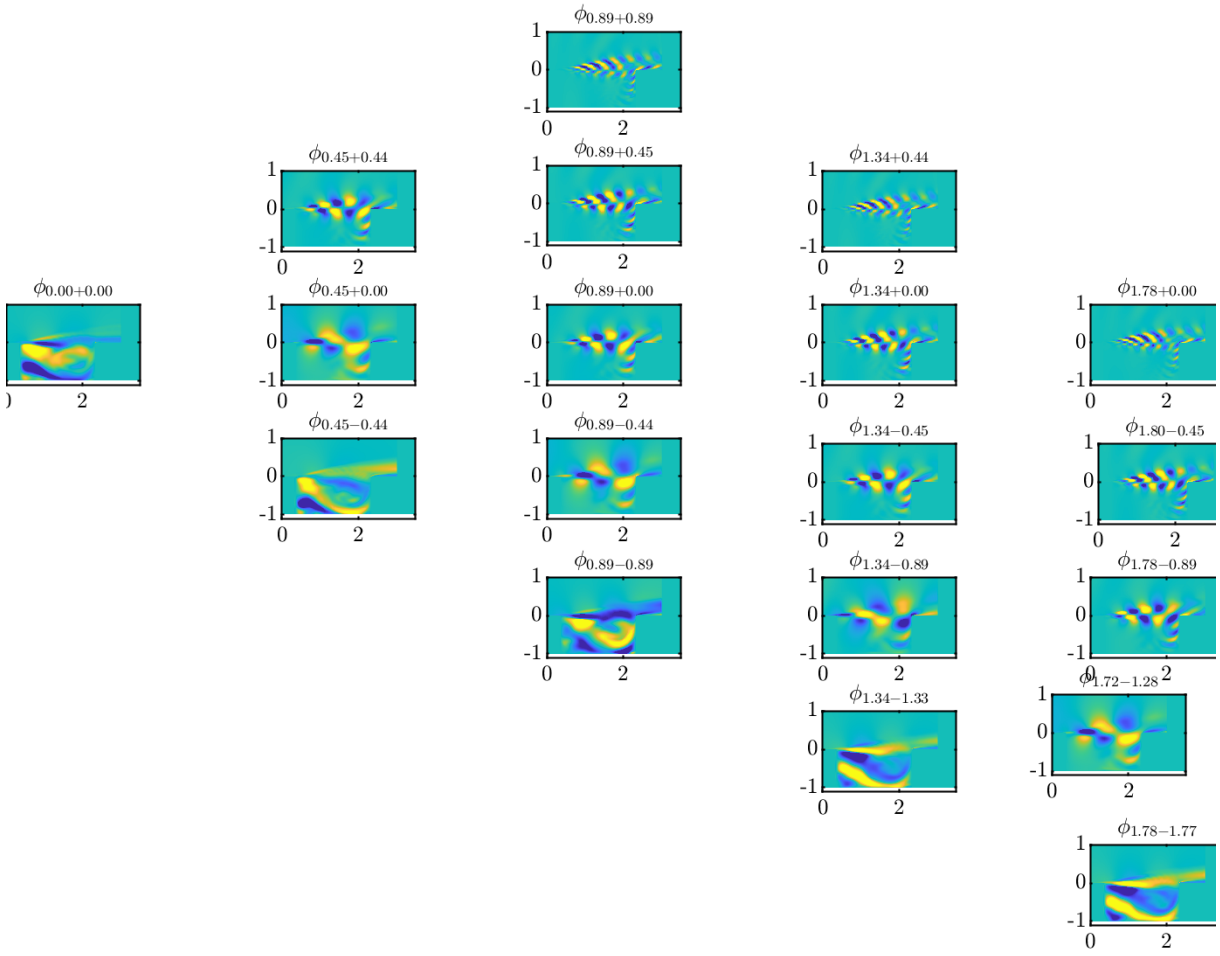

Figure A.4. Bispectral modes for spanwise wavenumber triplet $\{0, 1, 1\}$.

A.2 Spanwise Wavenumber Triplet $\{k_{z_1},\ k_{z_2},\ k_{z_1}+k_{z_2}=2\}$

This section contains all spanwise wavenumber triplets where $k_{z_1}+k_{z_2}=2$. For spanwise wavenumber triplet $\{0,2,2\}$, the peaks detected by the radial search algorithm in the summed mode spectrum shown in Figure A.6 are the same peaks as detected in Figure 3.5 with the exception of $f_3=0.0031$ being added. This summed mode spectrum is similar in order of magnitude compared to the spectrum for $\{0,1,1\}$. Double peaks can be found in the summed mode spectrum between Rossiter modes and a peak can be seen at $f_3=0.22$. Both energy transfer into and from f_3 can be found in this spanwise wavenumber triplet. Figure A.7 shows notable energy transfer terms in $f_3=0.0031$, which is close to the mean flow deformation $f_3=0$ and is interpreted as such. Once again, the largest energy transfers occur at the largest local maxima, with the largest energy transfer occurring at the first Rossiter mode and indicates energy into f_3. The magnitude of energy transfer is decreasing as the Rossiter mode increases, with a majority of the terms indicating energy from f_3.

For spanwise wavenumber triplet $\{1,1,2\}$, the peaks detected by the radial search algorithm in the summed mode spectrum shown in Figure A.10 are the same peaks as detected in Figure 3.5. Notably, this summed mode spectrum is weaker in order of magnitude compared to the spectrum for $\{0,1,1\}$. Double peaks can be found in the summed mode spectrum near the Rossiter modes and there is no longer a peak at $f_3=0.22$. Only energy transfer from f_3 can be found in this spanwise wavenumber triplet. Figure A.11 shows notable energy transfer terms in the mean flow deformation $f_3=0$. Once again, the largest energy transfers occur at the largest local maxima, with the largest energy transfer occurring at the mean flow deformation. The magnitude of energy transfer is decreasing as the Rossiter mode increases, with a majority of the terms indicating energy from f_3.

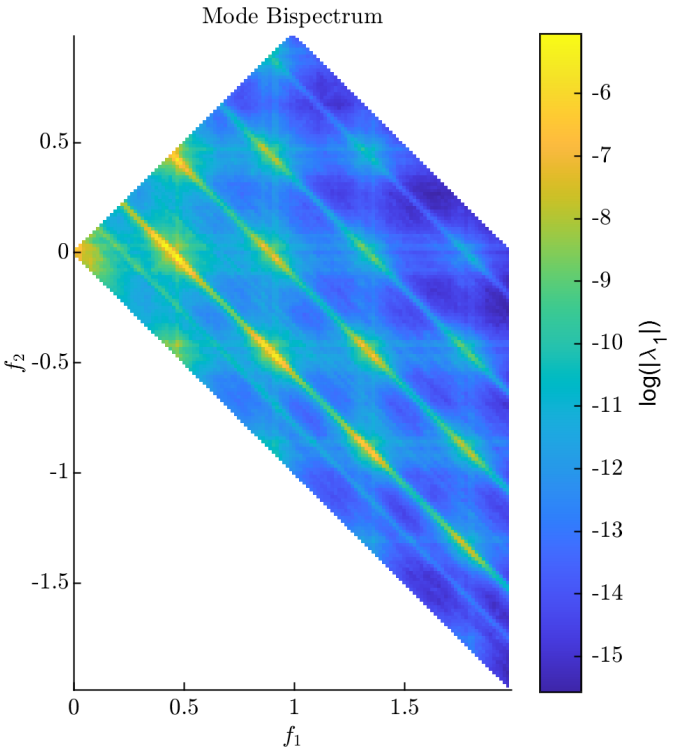

Figure A.5. Mode bispectrum for spanwise wavenumber triplet $\{0,2,2\}$.

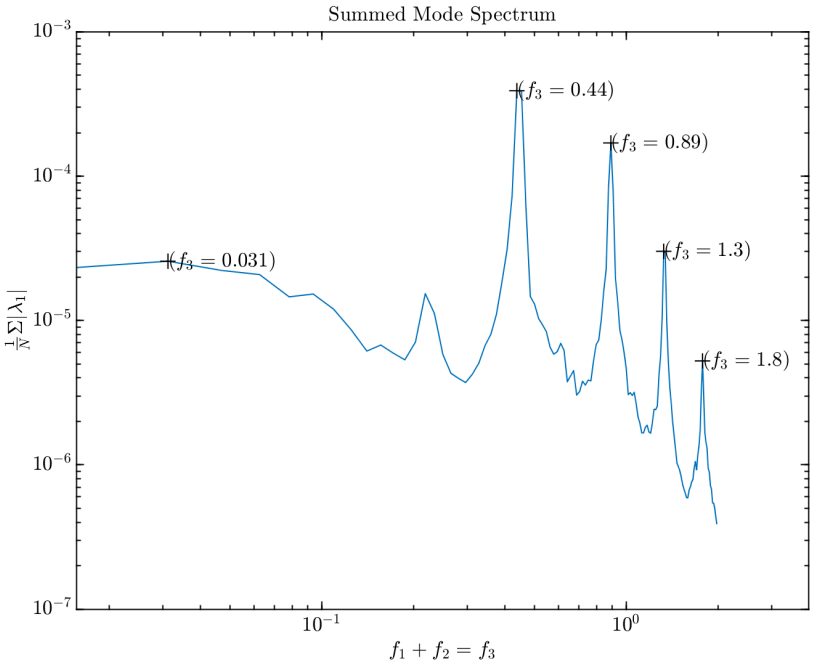

Figure A.6. Summed mode spectrum for spanwise wavenumber triplet $\{0,2,2\}$.

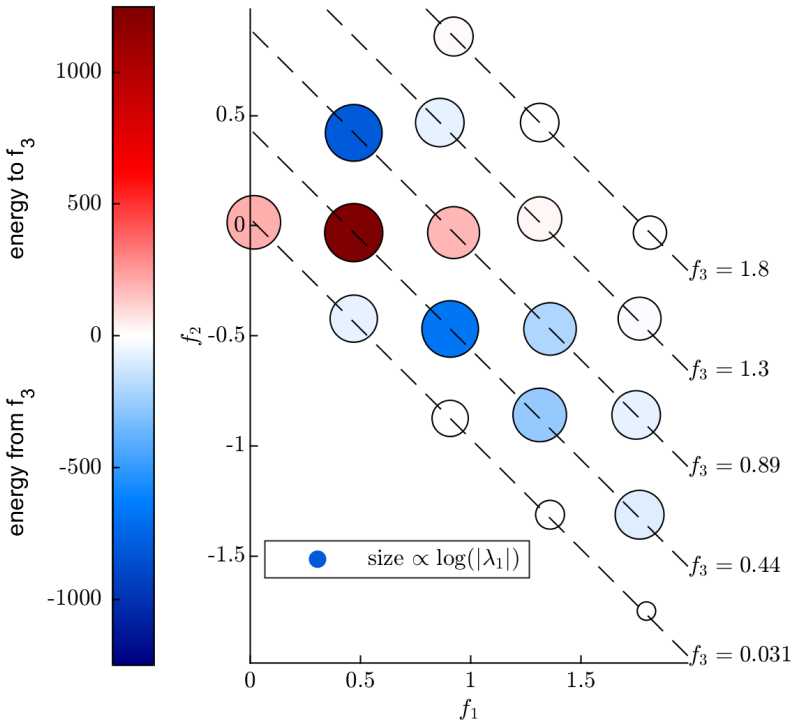

Figure A.7. Sparse mode bispectrum for spanwise wavenumber triplet $\{0, 2, 2\}$.

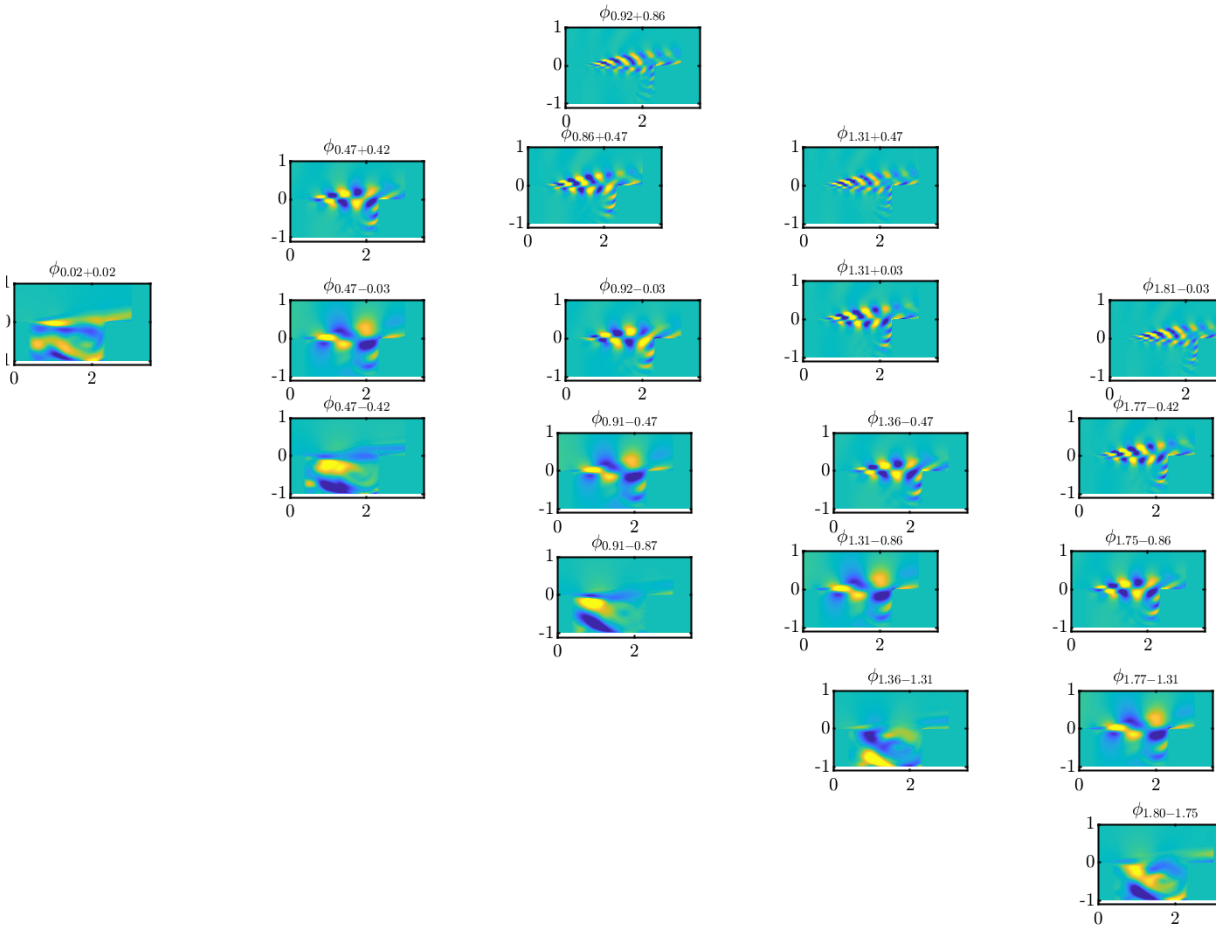

Figure A.8. Bispectral modes for spanwise wavenumber triplet $\{0, 2, 2\}$.

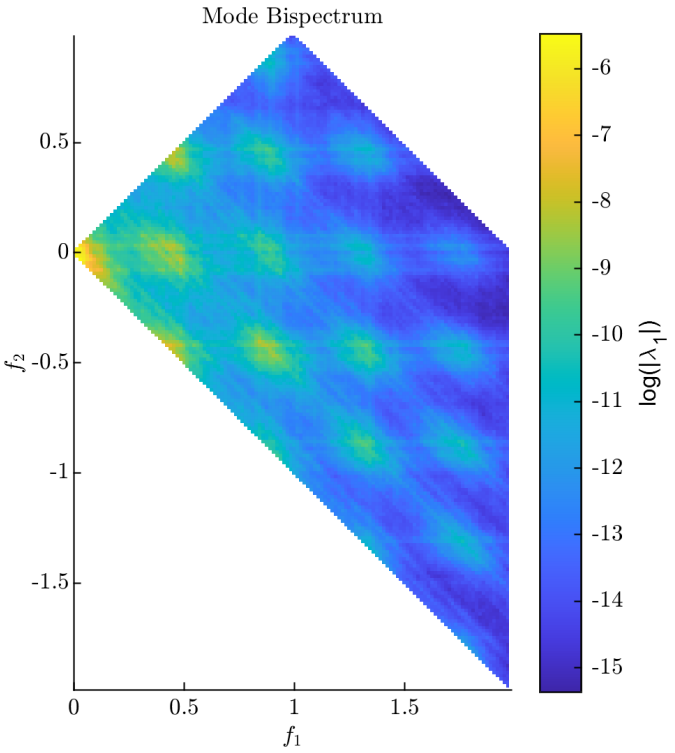

Figure A.9. Mode bispectrum for spanwise wavenumber triplet $\{1,1,2\}$.

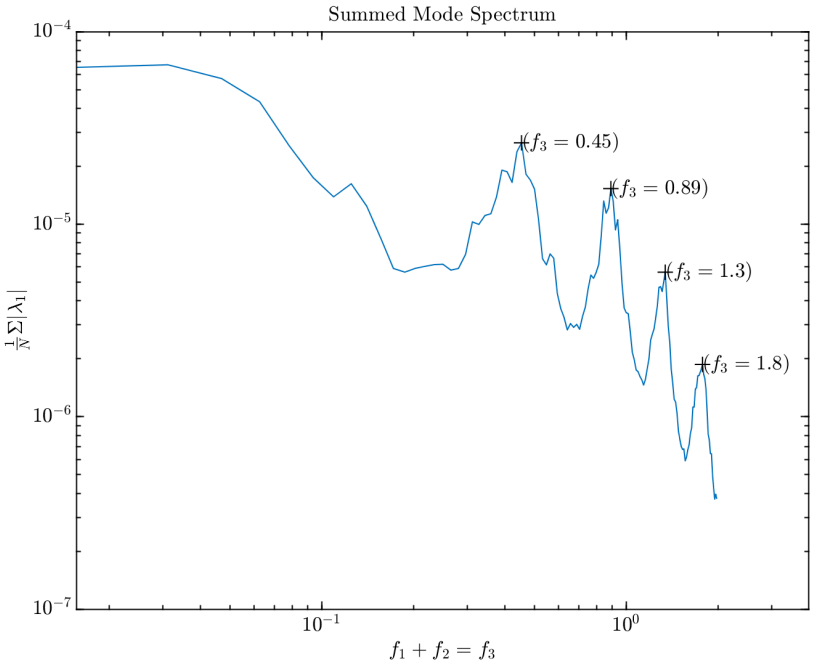

Figure A.10. Summed mode spectrum for spanwise wavenumber triplet $\{1,1,2\}$.

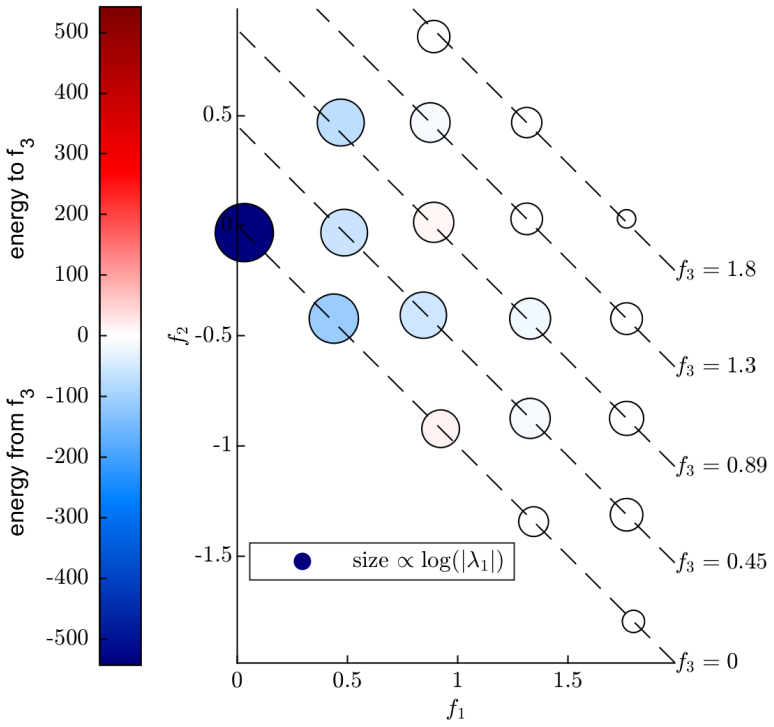

Figure A.11. Sparse mode bispectrum for spanwise wavenumber triplet $\{1, 1, 2\}$.

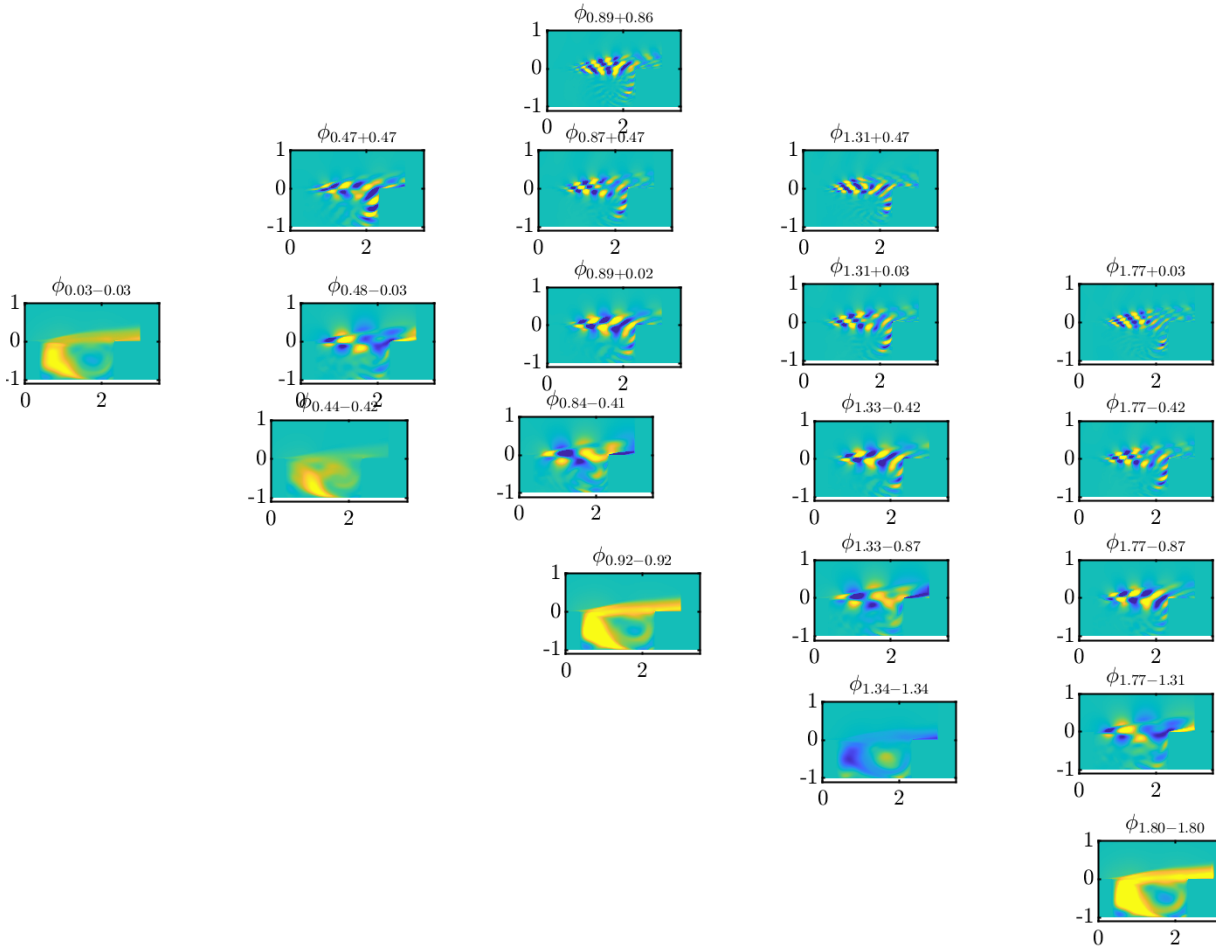

Figure A.12. Bispectral modes for spanwise wavenumber triplet $\{1, 1, 2\}$.

A.3 Spanwise Wavenumber Triplet $\{k_{z_1},\ k_{z_2},\ k_{z_1}+k_{z_2}=3\}$

This section contains all spanwise wavenumber triplets where $k_{z_1}+k_{z_2}=3$. For spanwise wavenumber triplet $\{0,3,3\}$, the peaks detected by the radial search algorithm in the summed mode spectrum shown in Figure A.14 are the same peaks as detected for $\{0,2,2\}$. This summed mode spectrum is similar in order of magnitude compared to the spectrum for $\{0,1,1\}$ and $\{0,2,2\}$. Double peaks can be found in the summed mode spectrum between Rossiter modes and a peak can once again be seen at $f_3 = 0.22$. Both energy transfer into and from f_3 can be found in this spanwise wavenumber triplet. Figure A.15 shows notable energy transfer terms in $f_3 = 0.0031$, which is close to the mean flow deformation $f_3 = 0$ and is interpreted as such. Once again, the largest energy transfers occur at the largest local maxima, with the largest energy transfer occurring at the first Rossiter mode and indicates energy into f_3. The magnitude of energy transfer is decreasing as the Rossiter mode increases, with a majority of the terms indicating energy into f_3.

For spanwise wavenumber triplet $\{1,2,3\}$, the peaks detected by the radial search algorithm in the summed mode spectrum shown in Figure A.10 are the same peaks as detected in Figure 3.5. Notably, this summed mode spectrum is weaker in order of magnitude compared to all previous spectrums. Double peaks can be found in the summed mode spectrum near the Rossiter modes and there is no longer a peak at $f_3 = 0.22$. Energy transfer into and from f_3 can be found in this spanwise wavenumber triplet. Figure A.19 shows notable energy transfer terms in the mean flow deformation $f_3 = 0$. Once again, the largest energy transfers occur at the largest local maxima, with the largest energy transfer occurring at the mean flow deformation. The magnitude of energy transfer is decreasing as the Rossiter mode increases, with a majority of the terms indicating energy into f_3.

From these additional results, we are able to draw a few conclusions. It appears the self-interaction wavenumber triplets $\{0,0,0\}$ and $\{1,1,2\}$ consist of only energy from f_3; no energy goes into f_3. The peak at $f_3 = 0.22$ seems to appear only when $k_z = 0$ is part of the

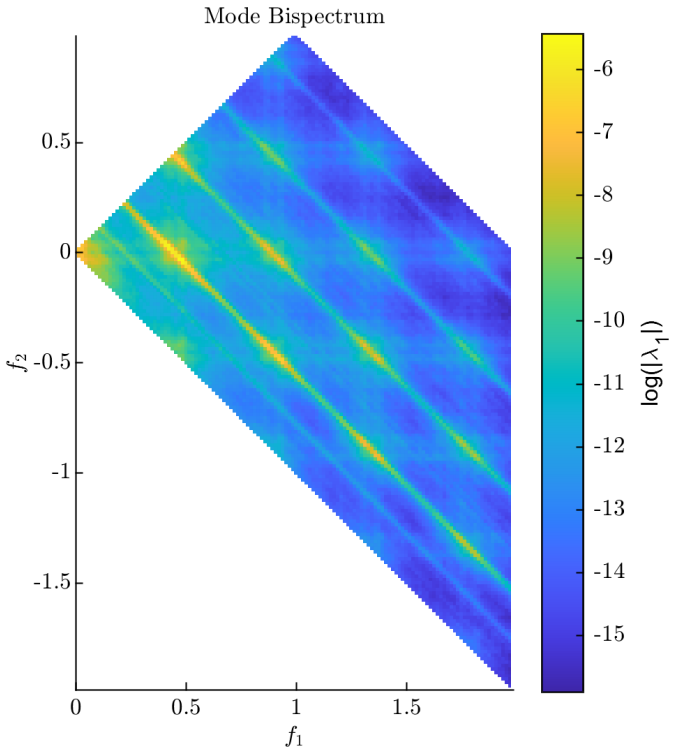

Figure A.13. Mode bispectrum for spanwise wavenumber triplet $\{0,2,2\}$.

wavenumber triplet, though there are no notable energy transfer terms found along this diagonal (searches with smaller f_r values were done to confirm this, but are not presented). Moreover, $k_z = 0$ leads to the double peak behavior in the summed mode spectrum occurring between the Rossiter modes rather than just before the modes. Spanwise wavenumber $k_z = 0$ also appears to have the largest impact on the summed mode spectrum's order of magnitude and implies $k_z = 0$ is the spanwise wavenumber most responsible for energy transfer. This is further reinforced by the magnitude of the energy transfer terms found in the sparse mode bispectrum. The energy transfer terms found in the sparse mode bispectrum for $\{0,0,0\}$ is three orders of magnitude larger than those found in $\{1,2,3\}$. Finally, the largest energy transfer always occurred at the largest local maxima for all sparse mode bispectrums, indicating that the mode bispectrum and energy transfer terms are related.

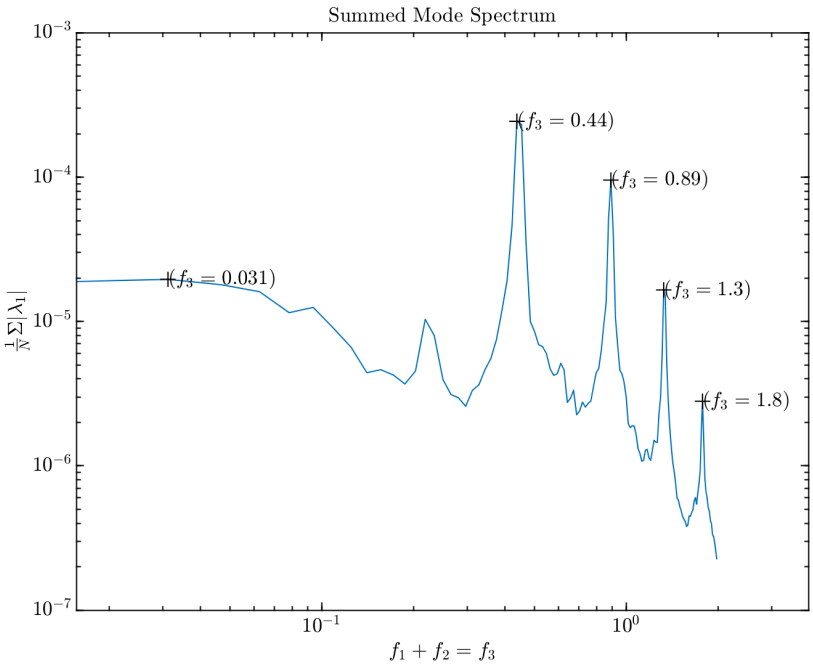

Figure A.14. Summed mode spectrum for spanwise wavenumber triplet $\{0, 3, 3\}$.

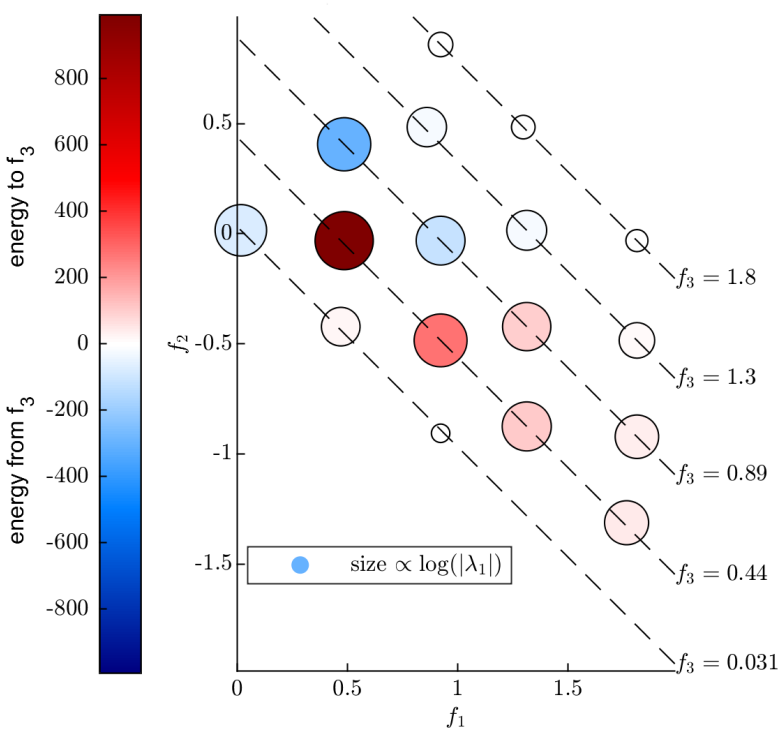

Figure A.15. Sparse mode bispectrum for spanwise wavenumber triplet $\{0, 3, 3\}$.

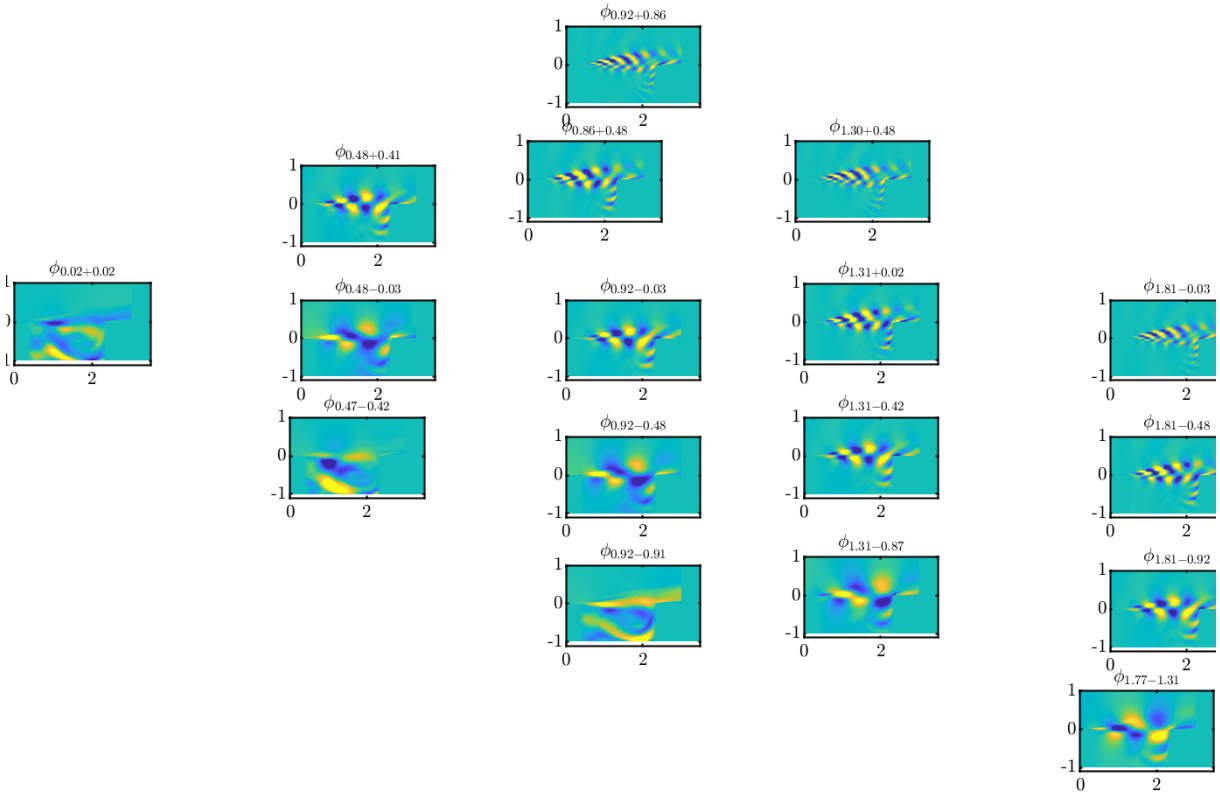

Figure A.16. Bispectral modes for spanwise wavenumber triplet $\{0, 3, 3\}$.

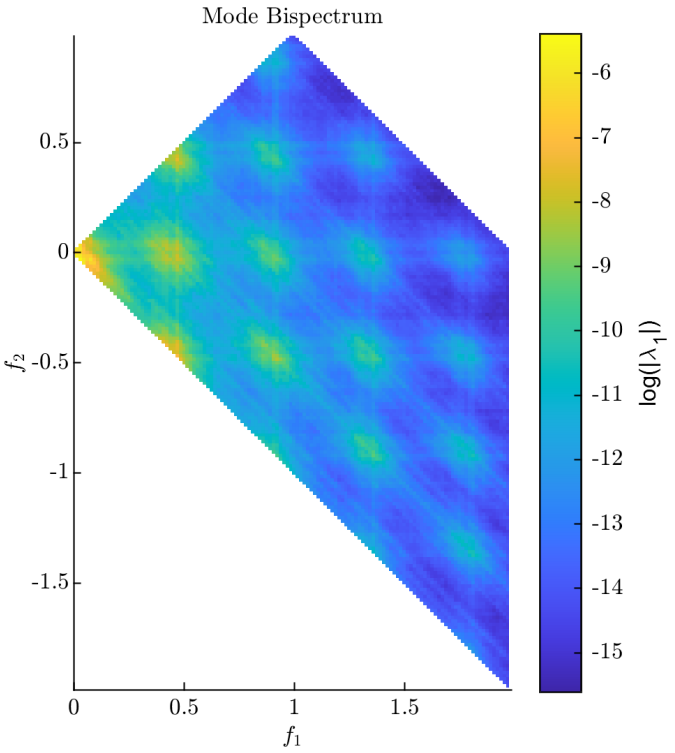

Figure A.17. Mode bispectrum for spanwise wavenumber triplet $\{1,2,3\}$.

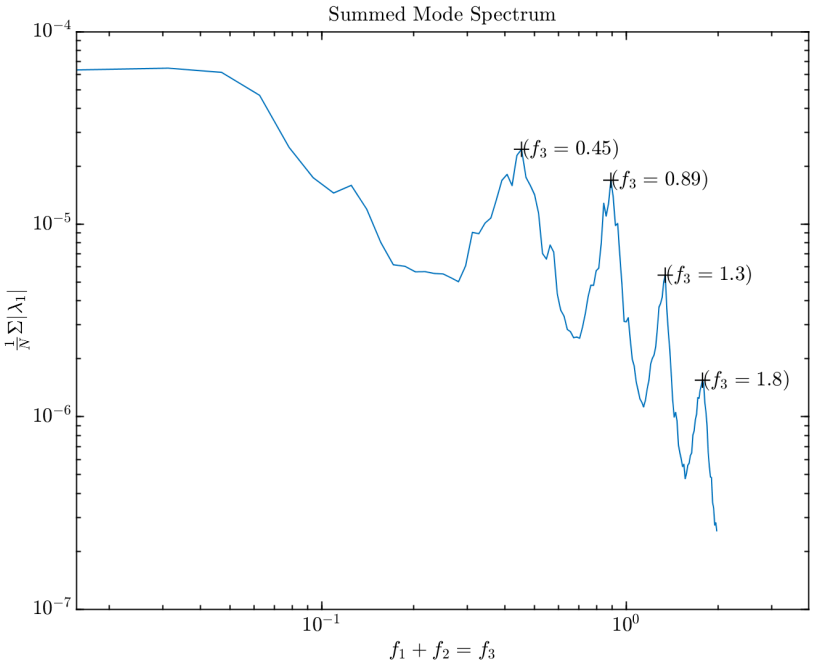

Figure A.18. Summed mode spectrum for spanwise wavenumber triplet $\{1,2,3\}$.

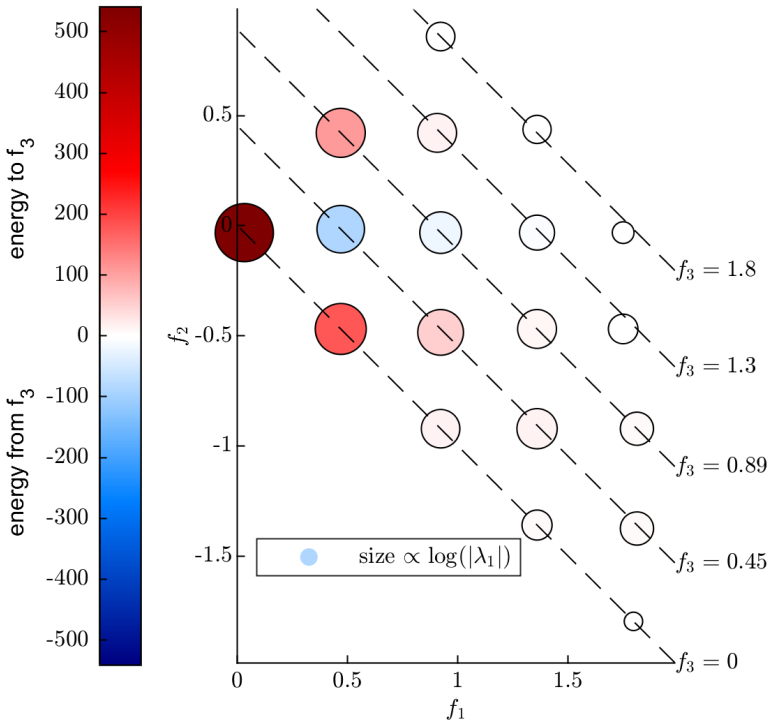

Figure A.19. Sparse mode bispectrum for spanwise wavenumber triplet $\{1,2,3\}$.

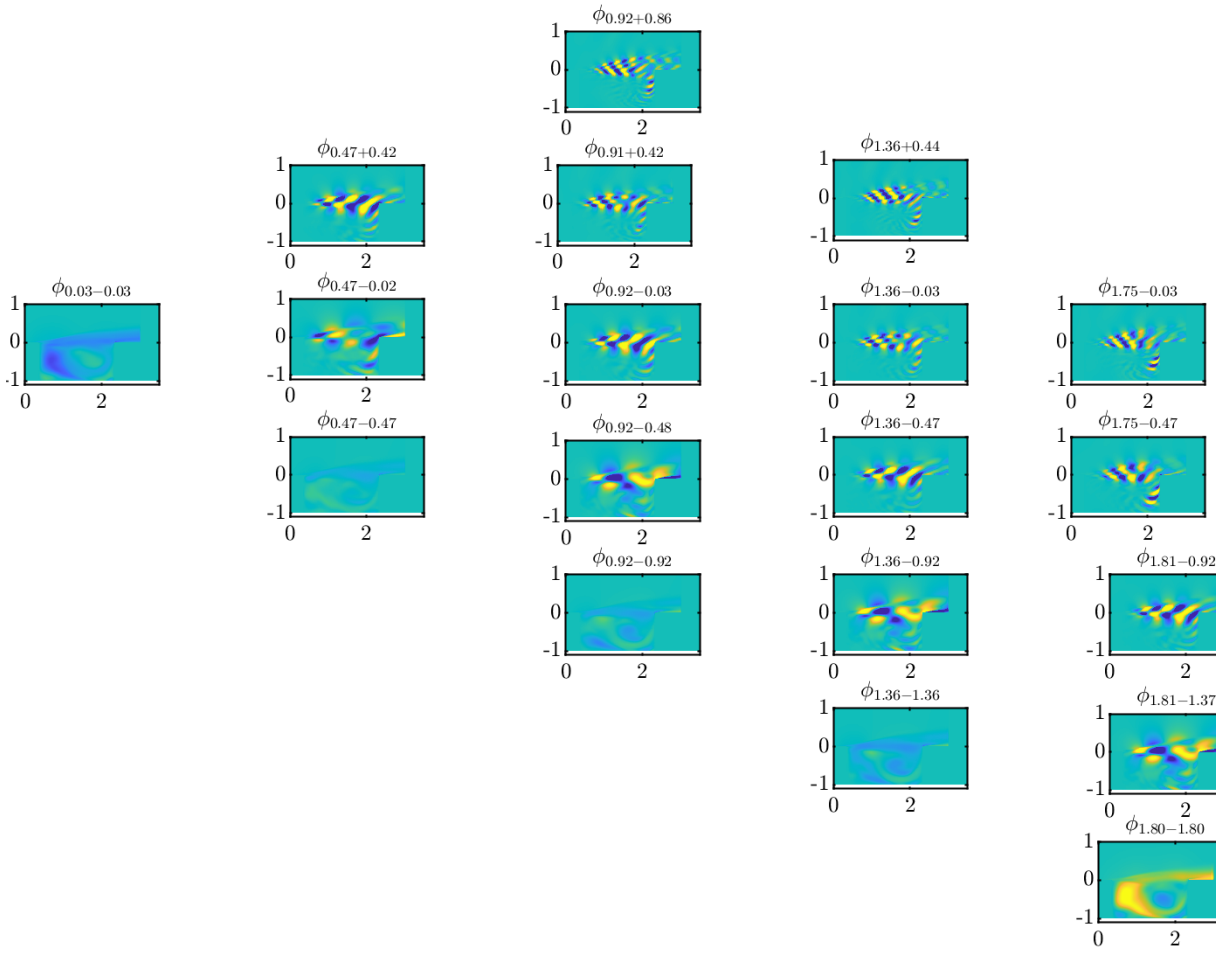

Figure A.20. Bispectral modes for spanwise wavenumber triplet $\{1, 2, 3\}$

Bibliography

[1] Anindya Chatterjee. An introduction to the proper orthogonal decomposition. *Current science*, pages 808–817, 2000.

[2] Nathan Childress. bluewhitered, 2003. URL: https://www.mathworks.com/matlabcentral/fileexchange/4058-bluewhitered.

[3] Gary N Coleman and Richard D Sandberg. A primer on direct numerical simulation of turbulence-methods. *procedures and guidelines*, 2010.

[4] J Andrzej Domaradzki and Robert S Rogallo. Local energy transfer and nonlocal interactions in homogeneous, isotropic turbulence. *Physics of Fluids A: Fluid Dynamics*, 2(3):413–426, 1990.

[5] Mohammad Farazmand and Themistoklis P Sapsis. A variational approach to probing extreme events in turbulent dynamical systems. *Science advances*, 3(9):e1701533, 2017.

[6] A Hamed, D Basu, A Mohamed, and K Das. Direct numerical simulations of high speed flow over cavity. *Proceedings (TAICDL), August*, pages 5–9, 2001.

[7] Chunyang He and GA Watson. An algorithm for computing the numerical radius. *IMA Journal of Numerical Analysis*, 17(3):329–342, 1997.

[8] The MathWorks Inc. Discrete fourier transform, 2023. URL: https://www.mathworks.com/help/signal/ug/discrete-fourier-transform.html.

[9] Michael A Kegerise, Eric F Spina, Sanjay Garg, and Louis N Cattafesta III. Mode-switching and nonlinear effects in compressible flow over a cavity. *Physics of Fluids*, 16(3):678–687, 2004.

[10] A Kolmogorov. Local structure of turbulence in an incompressible fluid at very high reynolds numbers. *CR Ad. Sei. UUSR*, 30:305, 1941.

[11] Robert H Kraichnan. Inertial ranges in two-dimensional turbulence. *The Physics of Fluids*, 10(7):1417–1423, 1967.

[12] Robert H Kraichnan. Inertial-range transfer in two-and three-dimensional turbulence. *Journal of Fluid Mechanics*, 47(3):525–535, 1971.

[13] E Leriche and S Gavrilakis. Direct numerical simulation of the flow in a lid-driven cubical cavity. *Physics of Fluids*, 12(6):1363–1376, 2000.

[14] Marlon Sproesser Mathias and Marcello Medeiros. Direct numerical simulation of a compressible flow and matrix-free analysis of its instabilities over an open cavity. *Journal of Aerospace Technology and Management*, 10, 2018.

[15] Marlon Sproesser Mathias and Marcello AF Medeiros. The effect of incoming boundary layer thickness and mach number on linear and nonlinear rossiter modes in open cavity flows. *Theoretical and Computational Fluid Dynamics*, 35(4):495–513, 2021.

[16] Emre Mengi and Michael L Overton. Algorithms for the computation of the pseudospectral radius and the numerical radius of a matrix. *IMA Journal of Numerical Analysis*, 25(4):648–669, 2005.

[17] PD Mininni, A Alexakis, and Annick Pouquet. Large-scale flow effects, energy transfer, and self-similarity on turbulence. *Physical Review E*, 74(1):016303, 2006.

[18] Lukas Moczarski, Nicholas C Treleaven, Kilian Oberleithner, Simon Schmidt, André Fischer, and Thomas L Kaiser. Interaction of multiple linear helical modes in the turbulent flow field of an industrial fuel injection system. In *AIAA SciTech 2022 Forum*, page 1061, 2022.

[19] Parviz Moin and Krishnan Mahesh. Direct numerical simulation: a tool in turbulence research. *Annual review of fluid mechanics*, 30(1):539–578, 1998.

[20] Lewis F Richardson. *Weather prediction by numerical process*. University Press, 1922.

[21] Horn Roger and R Johnson Charles. Topics in matrix analysis, 1994.

[22] JE Rossiter. Wind-tunnel experiments on the flow over rectangular cavities at subsonic and transonic speeds. *Tech. Rept.*, 1964.

[23] Peter J Schmid. Dynamic mode decomposition and its variants. *Annual Review of Fluid Mechanics*, 54:225–254, 2022.

[24] Peter J Schmid, Knud Erik Meyer, and Oliver Pust. Dynamic mode decomposition and proper orthogonal decomposition of flow in a lid-driven cylindrical cavity. In *8th International Symposium on Particle Image Velocimetry*, pages 25–28, 2009.

[25] Oliver T Schmidt. Bispectral mode decomposition of nonlinear flows. *Nonlinear dynamics*, 102(4):2479–2501, 2020.

[26] Oliver T Schmidt. bmd, 2023. URL: https://www.mathworks.com/matlabcentral/fileexchange/83408-bmd.

[27] Yiyang Sun, Aditya G Nair, Kunihiko Taira, Louis N Cattafesta, Guillaume A Bres, and Lawrence S Ukeiley. Numerical simulations of subsonic and transonic open-cavity flows. In *7th AIAA theoretical fluid mechanics conference*, page 3092, 2014.

[28] GA Watson. Computing the numerical radius. *Linear algebra and its applications*, 234:163–172, 1996.